




Article

The role of sulfate-rich fluids in heavy rare earth enrichment at the Dashigou carbonatite deposit, Huanglongpu, China

Delia Cangelosi^{1*} , Martin Smith², David Banks¹ and Bruce Yardley¹

¹School of Earth and Environment, University of Leeds, Leeds LS2 9JT, UK; and ²School of Environment and Technology, University of Brighton, Brighton BN2 4AT, UK

Abstract

The Huanglongpu carbonatites are located in the north-western part of the Qinling orogenic belt in central China. Calcite carbonatite dykes at the Dashigou open pit are unusual due to their enrichment in heavy rare earth elements (*HREE*) relative to light rare earth elements (*LREE*), leading to a flat *REE* pattern, and in that the majority of dykes have a quartz core. They also host economic concentrations of molybdenite. The calcite carbonatite dykes show two styles of mineralogy according to the degree of hydrothermal reworking, and these are reflected in *REE* distribution and concentration. The *REE* in the little-altered calcite carbonatite occur mostly in magmatic *REE* minerals, mainly monazite-(Ce), and typically have $\Sigma LREE/(HREE+Y)$ ratios from 9.9 to 17. In hydrothermally altered calcite carbonatites, magmatic monazite-(Ce) is partially replaced to fully replaced by *HREE*-enriched secondary phases and the rocks have $\Sigma LREE/(HREE+Y)$ ratios from 1.1 to 3.8. The fluid responsible for hydrothermal *REE* redistribution is preserved in fluid inclusions in the quartz lenses. The bulk of the quartz lacks fluid inclusions but is cut by two later hydrothermal quartz generations, both containing sulfate-rich fluid inclusions with sulfate typically present as multiple trapped solids, as well as in solution. The estimated total sulfate content of fluid inclusions ranges from 6 to >33 wt.% K₂SO₄ equivalent. We interpret these heterogeneous fluid inclusions to be the result of reaction of sulfate-rich fluids with the calcite carbonatite dykes. The final *HREE* enrichment is due to a combination of factors: (1) the progressive *HREE* enrichment of later magmatic calcite created a *HREE*-enriched source; (2) *REE*-SO₄²⁻ complexing allowed the *REE* to be redistributed without fractionation; and (3) secondary *REE* mineralisation was dominated by minerals such as *HREE*-enriched fluorocarbonates, xenotime-(Y) and churchite-(Y) whose crystal structures tends to favour *HREE*.

Keywords: *HREE*, carbonatite, sulfate, Huanglongpu

(Received 20 June 2019; accepted 25 November 2019; Accepted Manuscript published online: 11 December 2019; Associate Editor: Sam Broom-Fendley)

Introduction

The light rare earth elements (*LREE*; La to Sm) and the heavy rare earth elements (*HREE*; Eu to Lu) are now classified as critical raw materials by the European Commission (European Commission, 2017) due to the growing demand for these strategic elements. This has created a heightened interest in understanding the origin of economic *REE* deposits (Williams-Jones *et al.*, 2012; Wall, 2014).

Currently the largest and highest grade *REE* deposits are associated with carbonatite rocks (Chakhmouradian and Wall, 2012; Chakhmouradian and Zaitsev, 2012; Verplanck, 2017). Carbonatite deposits are commonly *LREE*-enriched (Woolley and Kempe, 1989; Rankin, 2005; Verplanck *et al.*, 2014), but a few carbonatite deposits, such as Huanglongpu (central Shanxi Province, China), the Lofdal complex (north-western Namibia)

and Bear Lodge (USA), show relative *HREE* enrichment (Xu *et al.*, 2007; Wall *et al.*, 2008; Andersen *et al.*, 2016). Many *REE* carbonatite deposits display evidence of hydrothermal reworking that can influence the final *REE* distribution and mineralogy (e.g. Smith *et al.*, 2000, 2015; Shu and Liu, 2019; Cangelosi *et al.*, 2019). Economic concentrations of *REE* are commonly hosted by minerals precipitated during hydrothermal alteration, rather than the early magmatic *REE* minerals (Wall, 2014).

This investigation follows from the recent work of Smith *et al.* (2018) on the Huanglongpu calcite carbonatites. They investigated the *HREE* enrichment of the carbonatites by looking at the progression from magmatic *REE*-bearing minerals to later hydrothermal *REE*-bearing minerals. They demonstrated that each subsequent *REE*-bearing mineral stage resulted in preferential leaching of the *LREE* and enrichment in the *HREE*. This is associated with a shift to more silica-rich hydrothermal conditions leading to quartz growth, and finally with sulfate mineralisation. They documented magmatic *HREE* enrichment seen in late-stage magmatic calcite. Subsequently, hydrothermal alteration of magmatic *REE* phases, notably monazite-(Ce), was accompanied by growth of secondary *REE* minerals, in particular britholite-(Ce) and Ca-*REE* fluorocarbonates, which show relative *HREE* enrichment compared to magmatic phases.

*Author for correspondence: Delia Cangelosi, Email: ee12dac@leeds.ac.uk

This paper is part of a thematic set arising from the 3rd International Critical Metals Conference (Edinburgh, May 2019).

Cite this article: Cangelosi D., Smith M., Banks D. and Yardley B. (2020) The role of sulfate-rich fluids in heavy rare earth enrichment at the Dashigou carbonatite deposit, Huanglongpu, China. *Mineralogical Magazine* 84, 65–80. <https://doi.org/10.1180/mgm.2019.78>

The Huanglongpu carbonatite is mined as a molybdenum deposit, but is considered to be part of a key *REE*-producing area of China, although its reserves and grades for the *REE* are unpublished (Kynický *et al.*, 2012). The presence of quartz with associated fluid inclusions, together with hydrothermal *HREE*-rich minerals, make it suitable for investigating the role of secondary hydrothermal fluid in the *REE* enrichment of carbonatites.

The Huanglongpu carbonatite deposit

Geological setting

The Huanglongpu deposit lies in the north-western part of the Qinling orogenic belt in central China (Xu *et al.*, 2007; Fig. 1). This orogenic belt hosts numerous ore deposits and is divided by the Shangdan suture into two parts: North and South Qinling. The northern border of the North Qinling belt is defined by a normal fault associated with the Cenozoic rift basin to the north. The southern Qinling belt is further divided by the Mianlue suture which was extensively reworked by Late Mesozoic thrusting (Xu *et al.*, 2010). A comprehensive summary of the North and South Qinling belt lithologies is given in Xu *et al.* (2010). The Qinling orogenic belt was incorporated into Rodinia during the Grenvillian orogeny, followed by rifting, then subduction-related tectonics in the Palaeozoic and early Mesozoic, leading to Cretaceous to Palaeogene reactivation, and finally Neogene extension. The detailed tectonic history can be found in Ratschbacher *et al.* (2003).

The Qinling orogenic belt is an important metallogenic belt, hosting the most important Mo ore camp in China and including several world-class Mo deposits (Mao *et al.*, 2008). The mineralisation is mostly hosted by granitic porphyry bodies with a few porphyry-skarn deposits. However, in the Huanglongpu area (Fig. 1) the Mo mineralisation is associated with unusual carbonatite veins. The Huanglongpu area contains an extensional structure hosting ore bodies that extend over a distance of 6 km, mainly controlled by a northwest-striking fault zone (Xu *et al.*, 2010; Fig. 1a). There are five ore fields currently being mined (Fig. 1a): Yuantou, Dashigou, Shijiawan I and II and Taoyuan, with a total reserve of 0.18 million tonnes of MoS₂. Apart from Shijiawan I, which is hosted by porphyry and has intruded into the Neoproterozoic Taihua gneiss, these are associated with carbonatite dykes. Most of the carbonatite ore fields are also related spatially to porphyry and porphyry skarn Mo deposits which yield Re–Os ages ranging from 148 Ma to 112 Ma (Mao *et al.*, 2008). However, the carbonatite molybdenite yields Re–Os ages from 209 Ma to 221 Ma and monazite-(Ce) U–Pb and Th–Pb ages from 208.9 ± 4.6 Ma and 213.6 ± 4.0 Ma (Huang *et al.*, 1994; Stein *et al.*, 1997; Song *et al.*, 2016) indicating that the mineralisation of the carbonatites is not related to overprinting by the porphyry-related systems. The samples analysed in this investigation are from the Dashigou open pit.

The Dashigou open pit

Individual molybdenite-bearing calcite carbonatite dykes at Dashigou are generally between 0.1 and 1 metre in width, and extend for several tens of metres (Fig. 1b). The main set of dykes predominantly dips N to NNW at steep angles, 50–88°N, (Smith *et al.*, 2018; fig. 1b). Regardless of the range of dyke orientations observed by Smith *et al.* (2018), including some east-dipping conjugate dykes, they are understood to be closely contemporaneous

(Smith *et al.*, 2018; fig. 3e). The country rock gneiss has been fenitised next to the carbonatites (Fig. 1c), and now consists mainly of K-feldspar, phlogopite, pyrite and calcite, with minor amounts of monazite-(Ce) and titanite. However, the fenite was apparently unaffected by the later hydrothermal alteration which corroded and altered monazite-(Ce) in the samples we studied.

Mineralogy of the calcite carbonatites

The carbonatite dykes are dominated by calcite and are referred to here as calcite carbonatite. The majority of the dykes contain central quartz lenses (Fig. 1c). A few dykes show evidence for multiple opening events (Table 1). The calcite carbonatite dykes consist of 50 to 80 vol.% calcite, with typical individual crystals ranging from less than 0.1 cm to 2 cm in size, together with sulfates (celestine–baryte), sulfides (molybdenite, pyrite, galena and sphalerite), K-feldspar, phlogopite, albite, *REE* minerals and apatite. Quartz only occurs as lenses and is only observed in the calcite carbonatite dykes and not the surrounding fenite. The lenses are composed of quartz grains, ranging from less than 100 µm up to 3 cm, containing µm-sized birefringent inclusions discussed later in this manuscript. Smith *et al.* (2018) described the paragenesis of the calcite carbonatite minerals. Molybdenite can occur as disseminated grains, as fracture infill within the calcite carbonatite, with other sulfides, or in fracture infill within the fenitised gneiss. Celestine–baryte was inferred to be hydrothermal in origin and Smith *et al.* (2018) documented a crosscutting relationship with the calcite carbonatite dykes. Pyrite and sphalerite are later than cogenetic molybdenite and pyrite.

The *REE* mineral assemblages of the calcite carbonatite dykes (Smith *et al.*, 2018) preserve a range of replacement textures making it possible to establish a history of *REE* mineral growth. The initial, magmatic stage associated with the calcite carbonatites consists of monazite-(Ce), bastnäsite-(Ce), parisite-(Ce) and aeschynite-(Ce) possibly with magmatic burbankite-(Ce); all these minerals are relatively enriched in *LREE*. Subsequent hydrothermal events first led the monazite-(Ce) to be altered to produce a second generation of apatite, and this was in turn replaced and overgrown by britholite-(Ce) accompanied by the crystallisation of allanite-(Ce). Bastnäsite-(Ce) and parisite-(Ce) were replaced by synchysite-(Ce) and röntgenite-(Ce). Aeschynite-(Ce) was altered to uranopyrochlore and then pyrochlore with uraninite inclusions (Smith *et al.*, 2018). These hydrothermal replacement minerals show *HREE* enrichment relative to the magmatic precursors.

The magmatic calcite shows some late *HREE* enrichment indicating that the Dashigou magmatic carbonatite system evolved to *HREE*-richer conditions (Xu *et al.*, 2007; Smith *et al.*, 2018). The composite dykes observed in the field suggest a sequence of calcite carbonatite pulses.

There is significant variation in the extent of hydrothermal alteration between calcite carbonatite samples, with magmatic *REE* phases well preserved in some, but mostly overprinted in others. Smith *et al.* (2018) concluded that the hydrothermal alteration was linked to the deposition of some of the quartz including the fluid inclusions which they host.

Methodology

Samples were collected from the Dashigou open pit in June 2016, within a 100 metre radius around location WGS84 49S, 410530E, 3803439N (Fig. 1a). The open pit exposes calcite carbonatite dykes intruded into country rock gneiss (Fig. 1). Four samples

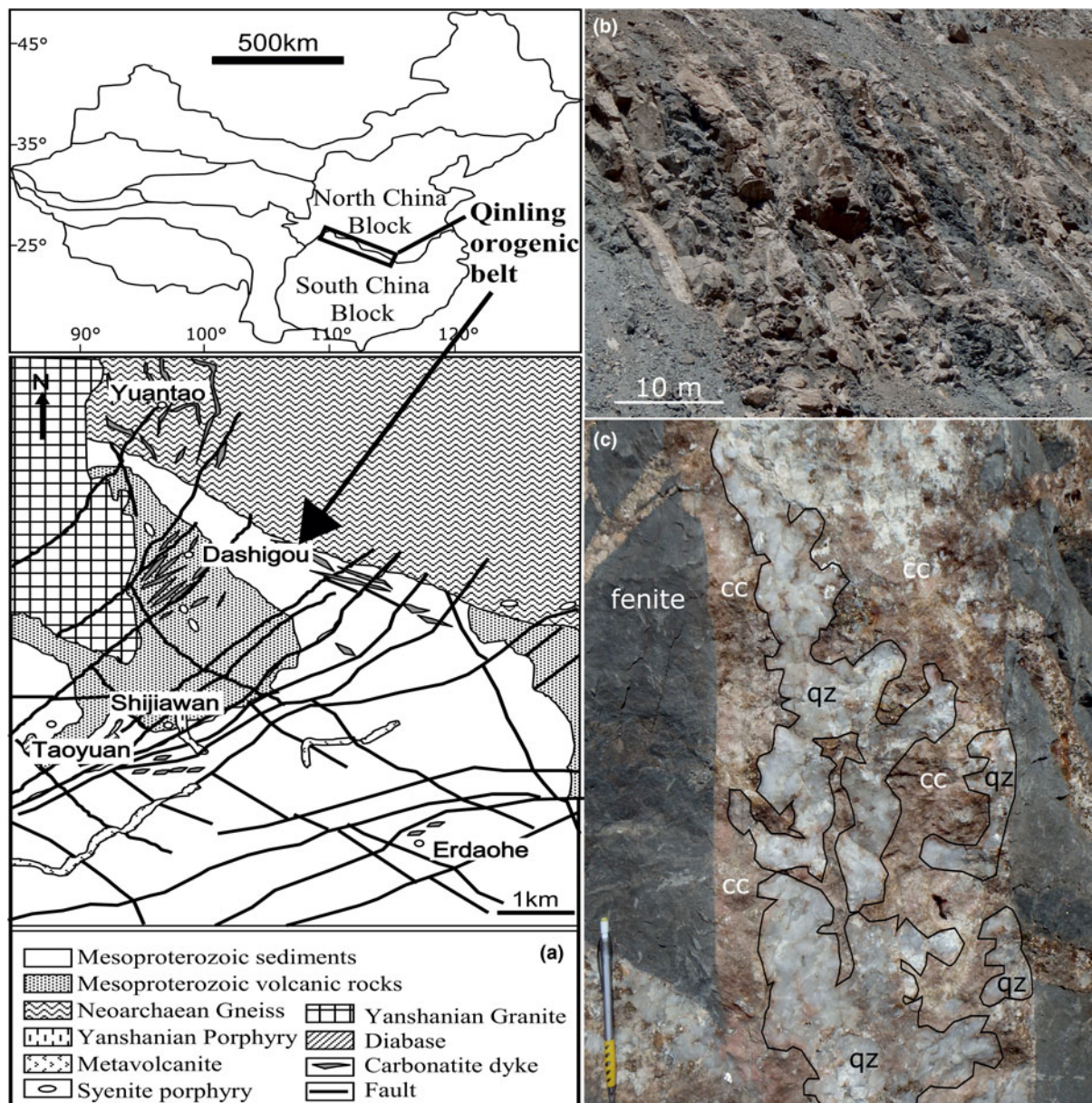


Fig. 1. (a) Geological map of the Huanglongpu Mo-district from Smith *et al.* (2018). (b,c) Examples of Dashigou open pit dykes, located around WGS84 410530 49S 3803439. (b) Set of parallel calcite carbonatite dykes at the Dashigou open pit. (c) Calcite carbonatite dyke with central quartz lenses and fenitised margins.

were also collected from the Yuantao mine dump a few kilometres north of the Dashigou open pit (WGS84 49S, 409886E, 3804124N). The two fenite samples used in this study were in direct contact with the associated calcite carbonatite samples.

Mineral and fluid-inclusion parageneses were established using optical petrography followed by scanning electron microscopy (SEM) at the University of Leeds using a FEI Quanta 650 field-emission gun scanning electron microscope operated at 20 kV employing back-scattered electron (BSE) and cathodoluminescence (SEM-CL) imaging.

Oxygen isotope measurements were undertaken on selected polished areas of some carbonatite samples mounted in an epoxy block. Prior to being mounted, the selected samples were mapped using BSE. Stable-oxygen-isotope measurements were carried out at the Edinburgh Ion Microprobe Facility (EIMF) using a Cameca 1270 mass spectrometer operating with a primary

Cs^+ beam, in multi collector mode, operating at conditions of ~ 5 nA with a net impact energy of 20 KeV (+10 kV primary and -10 kV secondary). The beam size was ~ 12 μm ; standards were: calcite (EIMF) and baryte (Stern S0237). The instrument was calibrated before each session and its drift was corrected by starting and finishing a session by analysing 5 to 10 points of the reference standards and then 5 points every ten analyses. Linear least squares was applied as the correction for drift. Reproducibility of the calcite and baryte standards can be found in Appendix 1 (Supplementary materials – see below).

Raman spectroscopy was carried out in the GeoResources Laboratory, at the University of Lorraine, France. The fluid-inclusion phases were analysed separately to identify solids and Raman-active solution and gas components. Analyses were performed using a LabRAM Raman microspectrometer (Horiba Jobin Yvon) equipped with a Linkam THMS600

Table 1. Summary of the Dashigou open pit samples used in this work. The alteration categories are based on the predominant *REE* minerals. ‘Little altered’ refers to samples with predominantly magmatic *REE* minerals and ‘altered’ refers to those with significant hydrothermal *REE* minerals (Smith *et al.*, 2018). Only DSG 007 and DSG 434 samples do not host quartz lenses.

Sample number	Field relationship	Dyke orientation	Alteration category
DSG 002	70 cm width calcite carbonatite dyke	252/77 N	Altered
DSG 004	50 cm width calcite carbonatite dyke	255/80 N	Altered
DSG 431	Six samples transect across complex 75 cm width multi-opening calcite carbonatite dyke. DSG 431 and DSG 436 are in contact with the fenite on each side	264/88 N	Little altered
DSG 432			Little altered
DSG 433			Altered
DSG 434			Altered
DSG 435			Little altered
DSG 436			Altered
DSG 437	10 cm width calcite carbonatite dyke	306/58 NE	Altered
DSG 437f	Fenite in direct contact with the calcite carbonatite dyke DSG 437		Little altered
DSG 005	50 cm width composite calcite carbonatite dyke	358/68 E	Altered
DSG 006	6 cm width calcite carbonatite dyke	355/84 S	Altered
DSG 007	4 cm width calcite carbonatite dyke	216/54 W	Little altered
ND 430-1	Three samples from the same calcite carbonatite dyke showing transition from the wall rock. ND 430-1 and ND 430-3 are in contact with the fenite on each side	<i>ex situ</i> boulder	Altered
ND 430-2			Altered
ND 430-3			Altered
ND 001f	Fenite in direct contact with the calcite carbonatite dyke ND 001		Little altered

microthermometry stage. The excitation beam was a monochromatic green laser at 514 nm (ionised argon 74.53 nm, with a working temperature of -128°C and a Pn of 500 mW). For each solid and gas analysis a spectrum was taken directly next to the fluid or solid inclusion to allow subtraction of the quartz and air N_2 peaks from the sample spectrum. The subtractions were made in Horiba *LabSpec* software, and *CrystalSleuth* software by RRUFF (Laetsch and Downs, 2006) was used to identify the solids. The gas proportions within the fluid inclusions were estimated using the method of Dubessy *et al.* (1989).

Microthermometry measurements were carried out at the University of Leeds using a Linkam MDS600 Heating Freezing Stage attached to a TMS93 temperature programmer and controller and an LNP cooling system mounted on an Olympus BX50 microscope. Double polished wafers were between 200–300 μm thick. The stage was calibrated using synthetic fluid-inclusion wafers containing pure water fluid inclusions (0°C and 374.1°C) and $\text{H}_2\text{O}-\text{CO}_2$ fluid inclusions (-56.6°C and 31.1°C) provided by Ronald Bakker, Leoben University, Austria.

Bulk rock analyses were carried out by Activation Laboratories Ltd. with the sample preparation undertaken at the University of Leeds. Samples were powdered using a steel pestle and mortar and an agate TEMA barrel and sieved to $<200\ \mu\text{m}$. The methods *4Litho* and *4F-Total sulfur* were used on the calcite carbonatite and country rock samples. The methods and detection limits are detailed in Appendix 1.

Results

Calcite carbonatites

The calcite carbonatite samples have been divided into two broad alteration categories, little altered and altered, based on the extent to which new *REE* minerals have replaced the original magmatic

ones (Table 1). No correlation of alteration with the different dyke orientations was observed. The little-altered samples host predominantly magmatic *REE* minerals. Monazite-(Ce) is the main primary magmatic *REE* mineral in the calcite carbonatite samples, and is usually fairly pristine in the little-altered samples (Fig. 2a), although in some instances it can show overgrowth and fracture-fill of late magmatic molybdenite (Fig. 2b). In the altered samples (Table 1) monazite-(Ce) is at least partially corroded and is sometimes fully replaced by new *HREE*-enriched phases (Fig. 2c), with later *HREE*-enriched phases in fractures (Fig. 2d). The *HREE*-enriched phases are predominantly Ca-*REE*-fluorocarbonates, uraninite, xenotime-(Y) and churchite-(Y) together with unidentified Y and *REE*-bearing silicate minerals with a variable amount of Ca and Fe, and unidentified Ti, Nb, U, Y and *REE*-bearing oxide phases with a variable amount of Fe and Ca (Fig. 2c) (Table 2). Smith *et al.* (2018) described the *REE* mineral paragenesis, demonstrating that the hydrothermal *REE* mineralisation becomes more *HREE* enriched with each subsequent hydrothermal event.

Xu *et al.* (2007) first reported that the Huanglongpu carbonatites are anomalously rich in the *HREE*, exhibiting a distinctive flat *REE* pattern. Xu *et al.* (2010) investigated calcite carbonatites from the Yuantou, Shijiawan and the Dashigou deposits and reported that total *REE* concentrations could exceed 3000 ppm. They found that $\Sigma\text{LREE}/(\text{HREE}+\text{Y})$ ratios ranged from 0.6 to 2.8. We have obtained a wider range of $\Sigma(\text{LREE}/\text{HREE}+\text{Y})$ ratios in this study, from 1.1 to 17.3, correlated with the alteration categories described above, with the little-altered calcite carbonatite samples showing $\Sigma\text{LREE}/\text{HREE}$ ratios ranging from 9.9 up to 17.3 and the altered calcite carbonatite samples ratios ranging from 1.1 to 3.8 (Table 3). $\Sigma\text{HREE}+\text{Y}$ totals also overlap with those reported by Xu *et al.* (2007; 2010).

The *REE* chondrite-normalised patterns for four little-altered calcite carbonatite samples in this study (DSG 431, DSG 431-2, DSG 007 and DSG 435; Tables 1, 3) are shown by blue lines on Fig. 3 and do not

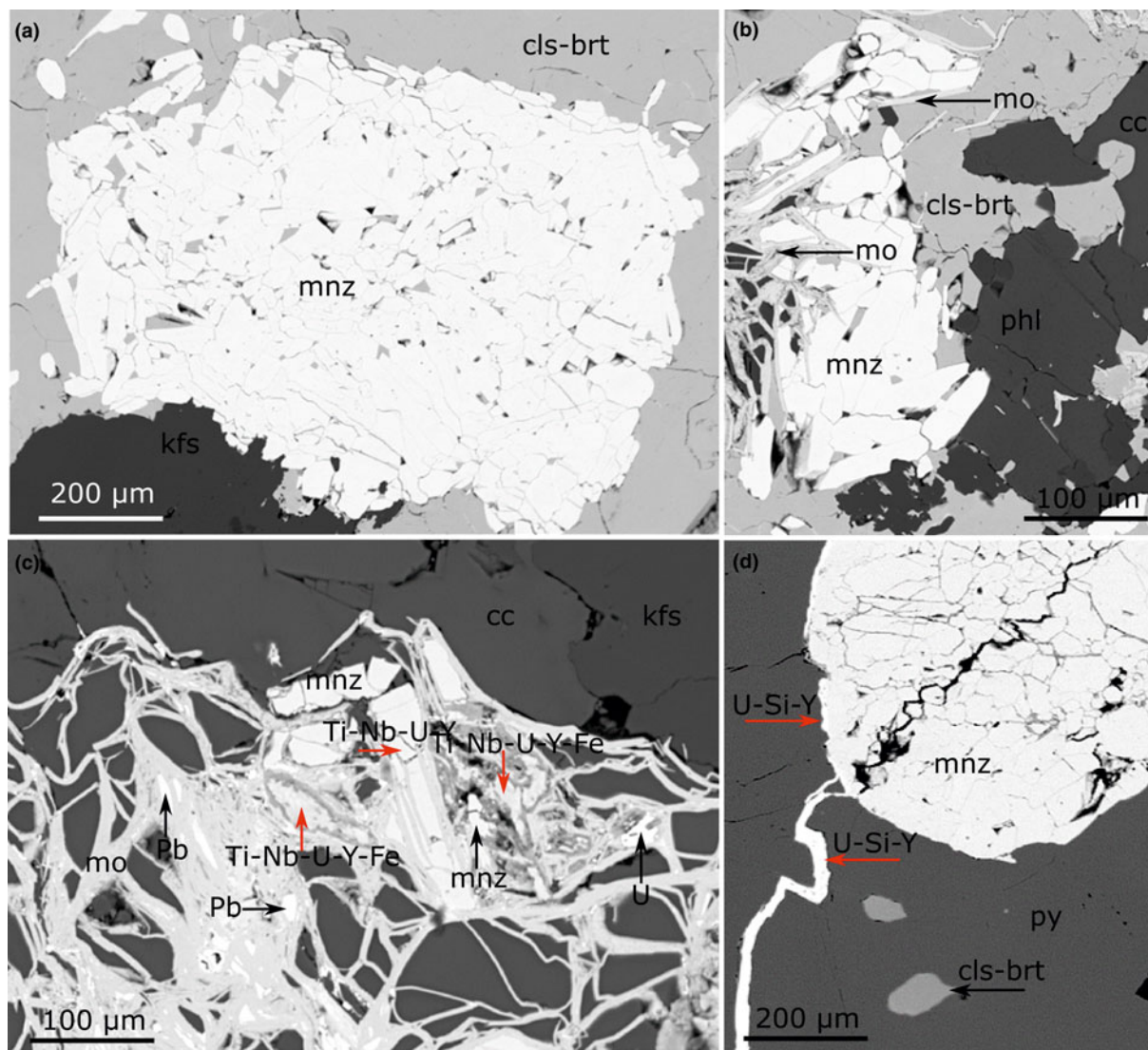


Fig. 2. Back-scattered electron images of magmatic monazite-(Ce) with different degrees of alteration. (a) Magmatic monazite-(Ce) and K-feldspar enclosed by hydrothermal celestine-baryte in a little-altered calcite carbonatite (DSG 431). (b) Magmatic phlogopite and monazite-(Ce) with overgrowth and fracture fill of molybdenite (DSG 431). (c) Magmatic monazite-(Ce) partially replaced by late magmatic molybdenite and an unidentified *HREE*-rich phase in an altered calcite carbonatite (DSG 434). (d) Magmatic monazite-(Ce) hosted by pyrite with a hydrothermal *Y*-rich phase in fractures and at the interface of monazite-(Ce) and pyrite grains, note associated hydrothermal celestine-baryte; altered calcite carbonatite (DSG 004). The red arrows in (c) and (d) indicate analysed points where the listed elements were the dominant constituents of unidentified hydrothermal phases. Abbreviation: cls-brt - celestine-baryte; mnz - monazite-(Ce); kfs - K-feldspar; mo - molybdenite; phl - phlogopite; cc - calcite; U - uraninite; Pb - lead metal; py - pyrite.

show the *HREE*-enrichment documented by Xu *et al.* (2010). Instead, they exhibit a *LREE*-enriched pattern typical of carbonatites worldwide (Woolley and Kempe, 1989) and similar to that of the fenites (Fig. 3, green lines). The fenite *REE* pattern reflects its *REE* mineralisation consisting mainly of unaltered monazite-(Ce), which has been observed in other carbonatite associated fenites (e.g. Thair and Olli, 2013; Midende *et al.*, 2014; Trofanenko *et al.*, 2016). In contrast, the altered calcite carbonatites in this study (Table 1, shown in red on Fig. 3) are *HREE*-enriched and plot close to the samples described by Xu *et al.* (2010) with the most *HREE*-enriched samples showing a positive *Y* anomaly (Fig. 3).

Quartz lenses within calcite carbonatite dykes

Irrespective of the host dyke's orientation, SEM-CL imaging reveals the presence of three quartz generations making up the

quartz lenses that occur within them (Fig. 4). The dominant generation is the earliest, Qz-1; it is moderately luminescent and shows some poorly-defined growth zonation. Generation Qz-2 occurs as non-luminescent overgrowths and porosity infills, merging into fracture fills cutting grains of Qz-1. The last generation, Qz-3, is also a non-luminescent quartz and occurs as thread-like fracture fills cutting both earlier generations. While Qz-1 lacks fluid inclusions and appears patchy and strained in cross polars, both Qz-2 and Qz-3 are cloudy and contain fluid inclusions.

Fluid-inclusion paragenesis and hydrothermal *HREE* mineralisation

Smith *et al.* (2018) showed that secondary quartz grew at the same time as the later hydrothermal *REE* minerals that are enriched in the *HREE*. The relationship between *HREE* minerals and Qz-2

Table 2. List of minerals encountered in this investigation and their occurrences.

Mineral	Formula	Occurrence
REE minerals		
Monazite-(Ce)	CePO ₄	Carbonatite rock
Uraninite	UO ₂	Carbonatite rock
Xenotime-(Y)	YPO ₄	Carbonatite rock
Churchite-(Y)	YPO ₄ ·2H ₂ O	Carbonatite rock
HREE enriched fluorocarbonate	-	Carbonatite rock
HREE enriched silicate	-	Carbonatite rock
HREE enriched oxide	-	Carbonatite rock
Sulfate minerals		
Celestine	SrSO ₄	Carbonatite rock/fluid inclusion
Baryte	BaSO ₄	Carbonatite rock/fluid inclusion
Arcanite	K ₂ SO ₄	Fluid inclusion
Anhydrite	CaSO ₄	Fluid inclusion
Aphthitalite	(K,Na) ₃ Na(SO ₄) ₂	Fluid inclusion
Glauberite	Na ₂ Ca(SO ₄) ₂	Fluid inclusion
Thénardite	Na ₂ SO ₄	Fluid inclusion
Anglesite	PbSO ₄	Fluid inclusion
Sulfides		
Pyrite	FeS ₂	Carbonatite rock
Galena	PbS	Carbonatite rock
Sphalerite	(Zn,Fe)S	Carbonatite rock
Molybdenite	MoS ₂	Carbonatite rock/fluid inclusion
Others		
Calcite	CaCO ₃	Carbonatite rock/fluid inclusion
Dolomite	CaMg(CO ₃) ₂	Fluid inclusion
Gypsum	CaSO ₄ ·2H ₂ O	Fluid inclusion
Apatite	Ca ₅ (PO ₄ ,CO ₃) ₃ (OH,F)	Carbonatite rock
Quartz	SiO ₂	Carbonatite rock
K-feldspar	KAlSi ₃ O ₈	Carbonatite rock
Phlogopite	KMg ₃ (Si ₃ Al)O ₁₀ (F,OH) ₂	Carbonatite rock
Albite	NaAlSi ₃ O ₈	Carbonatite rock
Muscovite	KAl ₂ (AlSi ₃ O ₁₀)(OH) ₂	Fluid inclusion
Whewellite	Ca(C ₂ O ₄)·H ₂ O	Fluid inclusion

and Qz-3 partially replacing magmatic calcite is shown in Fig. 5. HREE phases occur at the interface between calcite and Qz-2 (Fig. 5a) and in calcite fractures associated with celestine–baryte mineralisation related to Qz-3 (Fig. 5b).

Calcite and quartz stable oxygen isotope data

The samples analysed are from two distinct dykes and data is presented in Table 4. Secondary quartz data is from both Qz-2 and Qz-3 (non-luminescent quartz, Fig. 4) as these could not be distinguished during the analyses. Because of the difficulty in finding exact points for analysis in the ion probe, traverses were made across areas with all quartz generations to ensure that primary and secondary generations would be analysed. It is clear from the results that both Qz-1 and secondary quartz (Qz-2 and Qz-3) have similar compositions with tightly constrained populations of data that differ by no more than the analytical uncertainty (c. 0.25‰). Average compositions are close to 10‰ SMOW (e.g. DSG 002 Qz-1 δ¹⁸O ranges from 9.72‰ to 10.43‰ and secondary quartz δ¹⁸O ranges from 9.57‰ to 10.18‰; Table 4). Magmatic calcite has similar δ¹⁸O contents to quartz, averaging to 9.66‰ for sample DSG 437 and 10.34‰ for sample DSG

002. These figures are similar to calcite analysed by Bai *et al.* (2019) from the Huanglongpu and the Huangshui' carbonatites of the Lesser Qinling Orogen (δ¹⁸O ranges from 7.10‰ to 9.48‰).

Fluid-inclusion petrography and microthermometry

Three samples of quartz lenses from altered carbonatites were selected for the fluid-inclusion study (Fig. 3; Table 5): DSG 002, DSG 437 and DSG 433 (Table 1). Fluid inclusions range in size from <5 µm up to 70 µm but are commonly between 10 µm to 40 µm. Due to the cloudiness of Qz-2 and Qz-3, we were unable to collect freezing measurements such as T_{mCO₂} and T_{mCLA}. Fluid inclusions are abundant in Qz-2 and mainly occur as clusters or in fluid-inclusion-rich zones in cloudy quartz (Fig. 6a), more rarely in planar arrays and linear trails. The fluid inclusions usually have quite irregular shapes (Fig. 6a,b,d) and are predominantly LCO₂ + VCO₂ + Lw and LCO₂ + VCO₂ + Lw + S(s) type fluid inclusions (where LCO₂ = liquid CO₂, VCO₂ = gas CO₂, Lw = aqueous liquid and S(s) = from one to five solids). They show variable proportions of CO₂ relative to the aqueous liquid, even within the same fluid-inclusion cluster (Fig. 6a). Some inclusions have a homogenised CO₂ bubble at room temperature and are referred to as LCO₂ + Lw fluid inclusions (Fig. 6a; Table 5; Appendix 2). About 15% of the fluid inclusions in Qz-2 contain one or more solids (Fig. 6a–f; Tables 2,5). These solids are frequently birefringent and individual fluid inclusions can contain up to five different solids, but there is only ever one opaque solid (Fig. 6d). On rare occasions, fluid inclusions are not CO₂-bearing and only comprise an aqueous solution and solid(s) (Lw + S) with the solid taking up most of the inclusion volume. The Qz-2 generation may also contain small (<15 µm) birefringent solid inclusions near the fluid inclusions, within the same cluster or fluid-inclusion trail. These solid inclusions are of comparable size to the solids observed within the fluid inclusions (Fig. 6a).

Microthermometric data for Qz-2 fluid inclusions show a scatter of Th_{CO₂} from +12°C to +30.9°C, yielding a density of the CO₂ phase of 0.85 to 0.47 g cm⁻³ (Valakovich and Altunin, 1968). CO₂ always homogenised to the liquid phase.

In Qz-3, fluid inclusions occur in planar arrays decorating healed fractures (Fig. 6g–i) or as linear fluid-inclusion trails in finer healed fractures (<50 µm). Overall, the Qz-3 fluid inclusions are smaller than those in Qz-2 ranging from <5 µm to 25 µm. These fluid inclusions tend to have similar shapes within a single array, either elongate or with a more rounded shape (Fig. 6h–i). A wider variety of fluid-inclusion types are hosted by Qz-3 (Fig. 7) but they are predominantly of LCO₂ + VCO₂ + Lw type, similar to those in Qz-2, but with more variability in the relative proportion of the CO₂ and aqueous phase (Fig. 6h). Some of these fluid inclusions have a homogenised CO₂ bubble below room temperature. In aqueous inclusions (Lw + V) there is a reasonably constant liquid/vapour ratio (c. 80:20). Lastly, there are monophasic Lw inclusions which are small (<15 µm) and tend to occur in wider healed fractures, typically from 100 µm to 400 µm (Fig. 6i). They are clearly secondary. Lw and Lw + V type fluid inclusions can occur in the same fluid-inclusion trail and in this instance the vapour bubble proportion is usually lower at ~10% (Fig. 6i). Small (<15 µm) birefringent solid inclusions are also hosted by Qz-3, however they tend to be less abundant than in Qz-2.

For Qz-3, only five measurements of Th_{CO₂} on the LCO₂ + VCO₂ + Lw inclusions could be performed, ranging from 26.4°C

Table 3. Bulk rock compositions for the Dashigou open pit rocks described in Table 1.*

	DSG 002	DSG 004	DSG 431	DSG 431-2	DSG 432	DSG 433	DSG 434	DSG 435	DSG 436	DSG 005	DSG 437	DSG 437f	DSG 007	DSG 006
Major elements (wt.%)														
Total S	2.44	1.00	4.46	3.28	2.64	5.60	7.57	2.63	0.24	3.00	7.59	0.84	2.63	1.33
SiO ₂	19.15	5.42	9.53	65.54	69.43	13.20	13.57	77.54	6.61	13.67	14.03	46.96	74.84	13.41
Al ₂ O ₃	0.14	0.15	0.85	0.35	0.03	0.06	0.14	0.15	0.05	0.02	0.02	12.43	0.15	0.20
Fe ₂ O ₃ (tot.)	0.75	1.12	0.71	0.78	0.41	0.45	0.36	1.94	0.76	0.39	5.78	10.19	1.89	1.96
MnO	1.82	2.16	1.84	0.43	0.40	1.11	1.08	0.40	2.23	1.38	1.22	0.25	0.40	2.51
MgO	0.37	0.63	0.44	0.09	0.08	0.24	0.22	0.08	0.49	0.31	0.24	2.96	0.08	0.41
CaO	33.53	46.16	29.58	8.10	7.69	23.83	20.31	8.18	48.34	36.18	31.90	8.24	8.23	44.73
Na ₂ O	0.03	0.03	0.03	0.01	0.01	0.02	0.02	0.01	0.04	0.03	0.02	0.17	0.01	0.03
K ₂ O	0.10	0.13	0.73	0.30	0.03	0.05	0.13	0.13	0.04	0.02	0.01	10.65	0.12	0.14
TiO ₂	0.01	0.05	0.03	0.01	<0.01	<0.01	0.03	0.01	<0.01	<0.01	<0.01	1.50	0.01	0.01
P ₂ O ₅	0.06	0.09	0.27	0.04	<0.01	0.01	0.01	0.06	<0.01	<0.01	<0.01	0.57	0.07	<0.01
LOI	26.91	36.33	24.95	5.86	5.55	9.93	15.51	6.09	38.43	28.68	23.62	5.17	6.08	34.11
Partial total	82.88	92.28	68.95	81.51	83.63	48.89	51.39	94.59	97.00	80.69	76.84	99.09	91.88	97.51
Trace elements (ppm)														
Sc	3	7	5	1	1	4	2	1	5	2	1	21	1	3
V	<5	<5	<5	<5	<5	<5	<5	<5	<5	<5	<5	159	<5	<5
Ba	32,930	14,230	51,050	46,240	39,820	29,220	114,700	16,860	391	59,480	53,600	1562	19,570	1551
Sr	>10,000	>10,000	>10,000	>10,000	>10,000	>10,000	>10,000	>10,000	6094	>10,000	>10,000	746	>10,000	4472
Zr	4	<2	<2	<2	<2	<2	<2	<2	<2	<2	<2	180	<2	<2
Cr	<20	<20	<20	<20	<20	<20	<20	<20	<20	<20	<20	120	<20	<20
Co	<1	<1	<1	<1	<1	<1	<1	<1	<1	<1	<1	26	<1	<1
Ni	<20	<20	<20	<20	<20	<20	<20	<20	<20	<20	<20	40	<20	<20
Cu	10	20	30	<10	<10	40	<10	<10	<10	<10	<10	60	10	20
Zn	<30	<30	<30	<30	<30	<30	910	170	90	260	90	130	170	<30
Ga	<1	4	11	7	2	1	<1	6	5	5	<1	25	2	2
Rb	<2	3	7	3	<2	3	<2	<2	<2	<2	<2	186	<2	<2
Nb	10	44	19	2	<1	2	85	10	11	4	9	16	9	1
Mo	>100	>100	>100	>100	37	>100	>100	>100	>100	>100	>100	4	>100	17
La	508	531	1750	455	167	282	582	541	148	453	454	181	561	179
Ce	760	867	2620	589	125	387	476	794	385	617	522	321	810	422
Pr	69	80	221	49	9	37	37	68	51	65	53	32	68	52
Nd	235	271	658	142	32	140	123	197	223	251	212	110	199	218
Sm	40	48	73	18	8	31	27	21	61	52	42	18	19	46
Eu	13	15	19	7	5	12	15	5	18	17	15	5	5	14
Gd	43	50	45	12	9	36	30	12	66	43	36	13	12	44
Tb	7	8	6	2	2	6	6	2	11	6	5	2	1	7
Dy	46	51	37	10	10	39	36	8	67	35	30	10	8	40
Ho	11	11	8	2	2	8	8	2	14	7	6	2	2	9
Er	38	37	29	7	7	26	26	6	47	23	19	5	6	29
Tm	7	6	5	1	1	4	4	1	8	4	3	1	1	5
Yb	50	43	37	9	8	32	32	7	57	25	21	5	7	38
Lu	8	7	6	1	1	4	5	1	9	4	3	1	1	6
Y	466	437	318	75	73	244	235	54	472	217	198	53	53	348
Pb	30	19	116	178	3510	>10,000	396	656	7210	857	80	173	528	46
Bi	<0.4	<0.4	1	<0.4	4	138	2	4	4	1	0	<0.4	3	1
U	15	59	16	3	0	6	97	13	9	3	17	8	13	1
ΣLREE	1611	1797	5322	1252	342	877	1244	1621	868	1438	1283	662	1657	917
ΣHREE+Y	689	664	511	126	118	411	396	96	769	381	336	96	96	539
ΣLREE/HREE	2.3	2.7	10.4	9.9	2.9	2.1	3.1	16.9	1.1	3.8	3.8	6.9	17.3	1.7

*DSG 437f is the fenitized country gneiss associated with sample 437. '<' below detection limit of the instrument (detailed in Appendix 1). LREE = La to Sm, HREE = Eu to Lu + Y. Ge, Sb, In, Tl and Ta are under 2 ppm; As, Be, Sn, Cs and Hf are under 10 ppm and Ag and Th are under 20 ppm. Note that the total below 100% reflects the lack of data for Mo, Sr and F, which could be an important component of some samples. Compositional data for ND samples are detailed in Appendix 2.

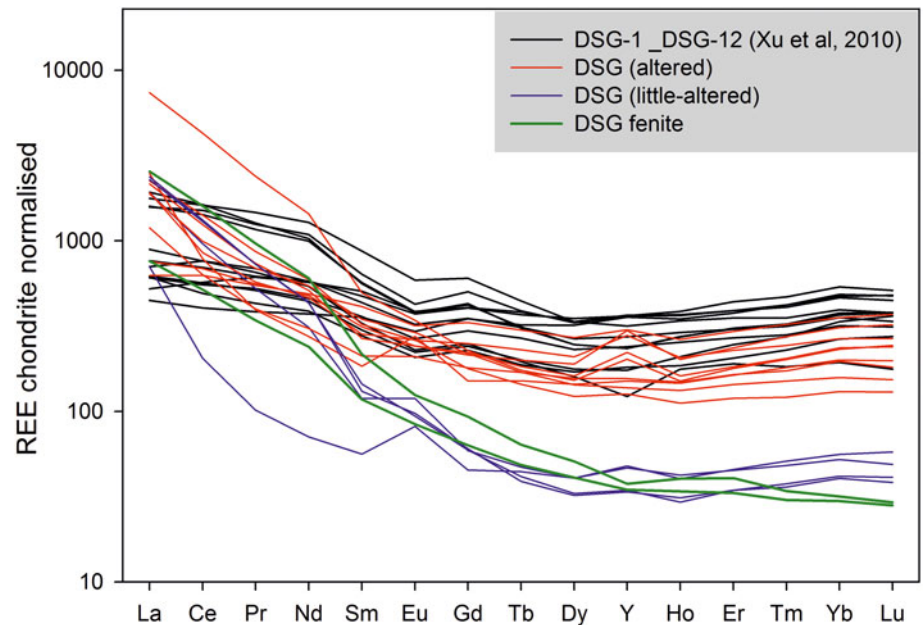


Fig. 3. REE chondrite-normalised patterns (McDonough and Sun, 1995) for calcite carbonatites (little hydrothermal alteration in blue and altered in red) and associated fenites (green lines). Samples with results from Xu *et al.* (2010) for the Dashigou open pit (alteration not specified, black lines) are shown for comparison. For details of the DSG samples investigated see Table 1.

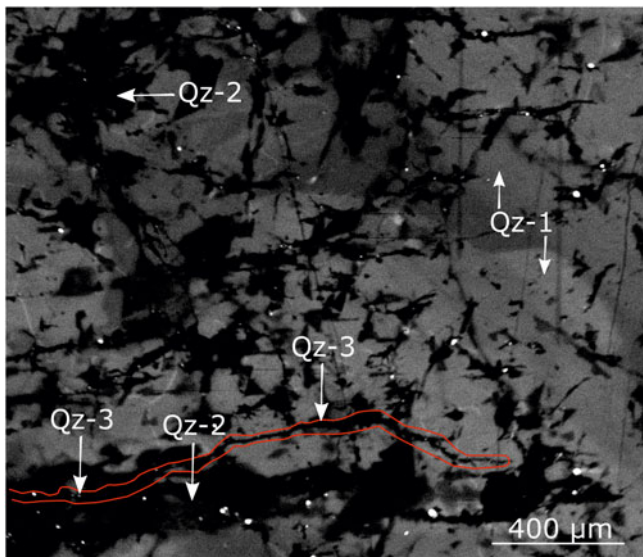


Fig. 4. SEM-CL image showing the paragenesis of the three quartz generations within a calcite carbonatite dyke, note the irregular zoning of the primary quartz (Qz-1) (DSG 005 001).

to 29.8°C corresponding to CO₂ densities of 0.70 g cm⁻³ to 0.56 g cm⁻³ (Valakovich and Altunin, 1968). Twenty Lw + V fluid inclusions show a temperature of total homogenisation (Th_{TOT}) ranging from ~120°C to 222°C. The Lw inclusions fail to nucleate a vapour bubble despite cooling to a temperature of -130°C for 5 min, something that is commonly indicative of low trapping temperature.

The sequence of the different types of fluid inclusions within Qz-3 is often ambiguous as cross-cutting relationships have not been observed. Nonetheless, in Qz-3 the Lw + V inclusions show a max Th_{TOT} of 222°C, and this is likely to be higher than the trapping temperature of the Lw inclusions, suggesting that they are probably not contemporaneous. The non CO₂-bearing fluid inclusions are inferred to be the youngest population (Fig. 7).

Raman spectroscopy

About 200 fluid inclusions were analysed from Qz-2 and Qz-3 in the three samples investigated (Table 5; Appendix 2). Compared to Qz-2, Qz-3, fluid inclusions are less suitable for Raman spectroscopy and microthermometric analysis as the majority are smaller than 20 μm. A summary of the fluid inclusion Raman spectroscopy data is provided in Appendix 2. When possible, the same fluid inclusions were analysed for solution, solid and gas. Both solid-bearing and solid-absent inclusions were analysed for solution components and gave comparable results.

Qz-2 fluid inclusions

The aqueous liquid phase of approximately 100 CO₂-bearing fluid inclusions was analysed by Raman spectroscopy. Sulfate (SO₄²⁻) ions were detected in solution in 90% of the fluid inclusions, from the peak at 981 cm⁻¹. A few inclusions without detectable sulfate in solution have sulfate solids and it is likely that where sulfate was not found this was a result of the small volume of liquid available. HSO₄ was not detected during the analysis (1050 cm⁻¹), precluding very acidic conditions (pH < 2).

In approximately 52 CO₂-bearing fluid inclusions, the vapour phase composition was determined. It is dominated by CO₂ and N₂ with CO₂ between 68% to 100%. Ninety percent of the fluid inclusions have a CO₂ content ≥95%. H₂S, CH₄ and H₂ were only detected as trace constituents (<1%) of the vapour phase. No difference in vapour phase composition was detected between solid-bearing inclusions and the inclusions without solids.

The majority of the solids hosted in the fluid inclusion in Qz-2 are sulfates (Fig. 8). They include arcanite, anhydrite, celestine, apthitalite and some other unidentified sulfates (Table 2); a few calcite crystals were also found (Figs 6a-f; 9). Note that celestine and glauberite have very similar Raman spectra and they can be hard to differentiate; when this was the case they are noted as celestine/glauberite in Appendix 2. Whewellite, thénardite, angle-site, dolomite, molybdenite, gypsum, muscovite and an unidentified phosphate mineral were also detected in fluid inclusions (Table 2). The opaque solids could not be identified as they moved under the laser beam.

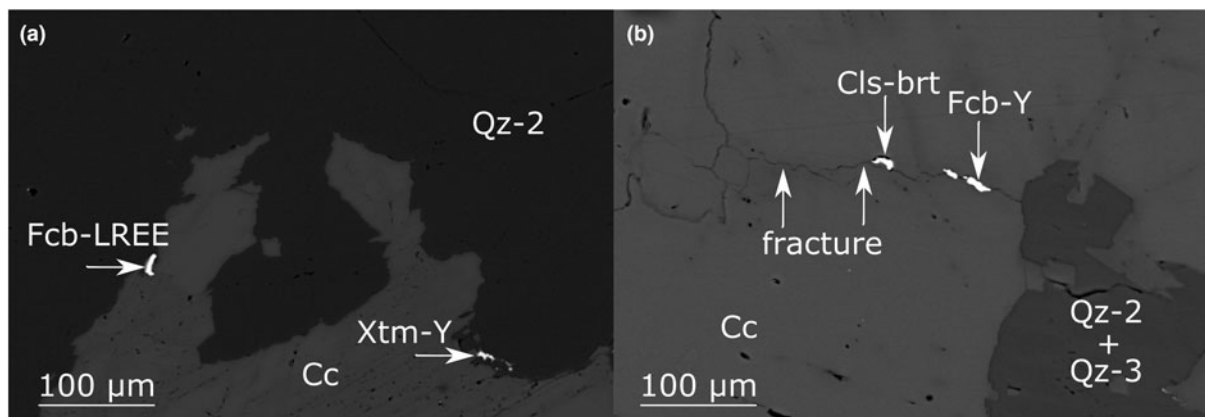


Fig. 5. BSE images of HREE enriched calcite carbonatite sample DSG 433. (a) HREE mineral hosted in hydrothermal Qz-2 at the interface with earlier calcite. (b) Mineralisation of a fracture in calcite by hydrothermal HREE minerals and celestine-baryte, inferred to be associated with the partial replacement of the calcite by quartz. Abbreviations: 'Fcb-LREE' - LREE fluorcarbonate; 'Xtm-Y' - Xenotime-(Y); 'Cc' - calcite; 'Cls-brt' - celestine-baryte.

Table 4. Summary of the oxygen isotope data from calcite and quartz, all as $\delta^{18}\text{O}$ SMOW.

Sample	DSG 437			DSG 002		
	calcite (‰)	Qz-1 (‰)	Qz-2/Qz-3 (‰)	calcite (‰)	Qz-1 (‰)	Qz-2/Qz-3 (‰)
$\delta^{18}\text{O}$ min	7.00	9.30	9.44	9.93	9.72	9.57
$\delta^{18}\text{O}$ max	10.14	11.03	10.32	10.81	10.43	10.65
Average	9.66	9.82	9.87	10.34	9.98	10.18
St. dev.	0.54	0.36	0.30	0.23	0.27	0.80
n	30	24	6	20	10	10

Solid inclusions also occur hosted directly in the quartz and these are predominantly sulfates (mainly anhydrite with one unidentified sulfate) and calcite.

Qz-3 fluid inclusions

Sulfate was only detected in about half of the 27 $\text{LCO}_2 + \text{VCO}_2 + \text{Lw}$ fluid inclusions analysed from Qz-3 (Table 5) and, as with Qz-2, fluid inclusions with and without detectable sulfate in solution occur within the same inclusion trails. Like Qz-2, CO_2 is the main component of the vapour phase, but in these inclusions is always >99%, with N_2 occurring in trace amounts only. The majority of the solid inclusions hosted directly in Qz-3 are calcite with some unidentified phosphate and sulfate particles (Fig. 8).

The aqueous portions of two Lw fluid inclusions were analysed and SO_4 was detected in both. About 75% of the 16 Lw fluid inclusions also had detectable sulfate in solution (Table 5).

Compared to Qz-2 fluid inclusions, Qz-3 fluid inclusions lack sulfate solids and sulfate is not always detected in solution. Likewise, there are fewer solid sulfate inclusions in Qz-3.

Fluid-inclusions origin and reconstructed composition

The $\text{LCO}_2 + \text{VCO}_2 \pm \text{Lw} \pm \text{S(s)}$ fluid inclusions in the Qz-2 and Qz-3 generations have variable $\text{CO}_2/\text{aqueous}$ phase ratios (Fig. 6a,h), from some that are nearly pure CO_2 inclusions to others than contain multiple solids, occurring in the same inclusion trails. This suggests that the fluid inclusions result from heterogeneous trapping of different phases that coexisted at the time of fluid-inclusion formation, including an aqueous liquid,

supercritical CO_2 and sulfate solids. Although the solids could be daughter minerals, formed after trapping during cooling of a homogeneous fluid, the compositional variability (Figs 5; 7) and the fact that they show no signs of dissolution during heating before the inclusions decrepitate between 225°C to 325°C, makes this unlikely. Accidental trapping is the preferred interpretation, particularly as some of the same solid phases also occur in the quartz as solid inclusions of similar size (Fig. 6a). We infer that these solids were present in the fluid while Qz-2 was being precipitated. Hence, the composition of these inclusions does not represent any single fluid. Regardless of this limitation, we have attempted to estimate the compositions of a number of the individual inclusions.

Due to the chemically complex sulfate-rich fluid and sulfate solids within the fluid inclusions, interpretation of the microthermometric measurements is problematic due to the lack of knowledge of the precise chemical system. The presence of sulfate crystals in these fluid inclusions precludes conventional estimation of their dissolved load as NaCl equivalent salinity. Instead, we used visual proportion estimates to calculate the bulk composition of individual solid-bearing fluid inclusions (Shepherd *et al.*, 1985; Fig. 6a; Appendix 2). Due to the clear evidence of heterogeneous trapping, these estimates represent the composition of the material trapped in the fluid inclusions, not a true fluid composition.

Fluid inclusion DSG 002 4 (Fig. 6a) is a $\text{LCO}_2 + \text{VCO}_2 + \text{Lw} + \text{S}$ fluid inclusion hosting a single crystal of arcanite consisting of 15% of the inclusion by volume, with 15% CO_2 -rich vapour phase and 70% arcanite-saturated aqueous phase (the volumes were estimated using visual proportion estimates as presented in Appendix 2). These proportions give a bulk fluid-inclusion composition of 33 wt.% K_2SO_4 equivalent or ~ 3 molal K_2SO_4 . Some other solid-bearing fluid inclusions have multiple sulfate crystals taking up >15% of the fluid-inclusion volume and must therefore have an even higher sulfate content (Fig. 6). The sulfate-bearing $\text{LCO}_2 + \text{VCO}_2 + \text{Lw}$ fluid inclusions hosted in Qz-2 have similar petrographic characteristics to the $\text{LCO}_2 + \text{VCO}_2 \pm \text{Lw} \pm \text{S(s)}$ fluid inclusions. Hence, their salinities have also been estimated as equivalent K_2SO_4 using the visual estimate proportion method assuming a K_2SO_4 saturated solution. The majority of these fluid inclusions have the CO_2 bubble occupying from 10% to 60% of the fluid inclusion. This corresponds to a salinity between 6–10 wt. % K_2SO_4 equivalent, or <0.7 molal K_2SO_4 .

Table 5. Summary of the different fluid-inclusion types and their characteristics measured by microthermometry and Raman spectroscopy.

Fluid-inclusion type	Occurrence	Microthermometry	Anion in solution	Solid within fluid inclusion	Gas component
LCO ₂ + VCO ₂ + Lw/LCO ₂ + Lw	Qz-2	Th _{CO₂} = 12.0°C to 30.9°C	SO ₄ ²⁻	n.a.	CO ₂ varies from 68% to 100% with N ₂ ; trace of H ₂ S, CH ₄ and H ₂
LCO ₂ + VCO ₂ + Lw + S(s)	Qz-2	Th _{CO₂} = 12.0°C to 30.9°C	SO ₄ ²⁻	Mainly: arcanite, anhydrite, celestine, glauberite, apthitalite, unidentified sulfate, calcite. Few: whewellite, thénardite, anglesite, dolomite, molybdenite, gypsum, muscovite, unidentified phosphate.	" "
LCO ₂ + VCO ₂ + Lw/LCO ₂ + Lw	Qz-3	Th _{CO₂} = 26.4°C to 29.8°C	SO ₄ ²⁻ in 55%	n.a.	CO ₂ >99% with trace of N ₂
Lw + V	Qz-3	Th _{TOT} = 120.0°C to 222.3°C	SO ₄ ²⁻ in 65%	n.a.	n.a.
Lw	Qz-3	n.a.	SO ₄ ²⁻ in 75%	n.a.	n.a.

Interpretation and discussion

Origin of the quartz lenses

The systematic localisation of the quartz lenses within the dyke cores (Fig. 1) indicates they are genetically linked to the calcite carbonatite and formed in the same stress field, which is consistent with the lack of quartz lenses in the surrounding rocks. The quartz lenses are not intergrown with the calcite indicating they are not conventional magmatic phases.

Both Qz-2 and Qz-3 are believed to be of hydrothermal origin due to the volume for volume replacement texture observed, their characteristic non-luminescent CL emission (Fig. 4) and the presence of fluid inclusions. The Qz-3 Lw + V fluid inclusions Th_{TOT} temperatures point to low hydrothermal temperatures (120–222°C).

The origin of the original quartz (Qz-1 in this study) from the Huanglongpu calcite carbonatites, which accounts for just over 50% of the quartz lenses in our samples overall, has been discussed by Song *et al.* (2015). They suggested a magmatic origin of the quartz from Si enriched carbonatitic liquids which might have been produced by intensely fractional crystallisation of non-silicate minerals. Bai *et al.* (2019) expanded on the work of Song *et al.* (2015) and concluded that quartz precipitated mainly before calcite, which is consistent with the calcite veins locally cross-cutting the quartz lenses observed in this study, but must also be reconciled with the fact that quartz lenses only occur within calcite carbonatite dykes. Bai *et al.* (2019) also favoured a magmatic origin, but they ascribed the coarse, nearly monomineralic quartz grains to a supercritical C–H–O–Si magmatic fluid intermediate between a hydrous melt and an aqueous solution. Our stable oxygen isotope data (Table 4) indicates very small fractionation between quartz and calcite, which is indicative of temperatures in excess of 500°C (Zheng, 1999) and is consistent with a magmatic environment (Table 4). We conclude that the quartz veins formed from a fluid of magmatic origin, but were subsequently reworked by hydrothermal activity.

Conditions of hydrothermal activity

There is no direct measurement of the temperature of Qz-2 and Qz-3 precipitation but the quartz luminescence and the fluid inclusions provide some indications. The brighter luminescence of Qz-1 compared to the later quartz generations indicates a higher temperature for growth. The later quartz generations exhibit low CL emissions, typical of hydrothermal quartz (Rusk and Reed, 2002; Rusk *et al.*, 2006). Both Qz-2 and Qz-3 show

very similar luminescence (Fig. 4) and on the basis of the literature on non-luminescent hydrothermal quartz precipitation, they have probably precipitated at temperatures below ~450°C.

The CO₂-bearing fluid inclusions hosted in Qz-2 and Qz-3 decrepitated upon heating before homogenisation. It is likely that decrepitation only occurs above the temperature of trapping and, if so, the maximum trapping temperature is below the range 225 to 325°C. The homogenisation temperature Th_{TOT} of the Lw + V fluid inclusions hosted in Qz-3 give a temperature range from 120 to 220°C which may be close to the true trapping temperature as the system was experiencing significant fluid flow. This is consistent with the low luminescence from Qz-2 and Qz-3 (Fig. 4) and with the association of hydrothermal bastnäsite-(Ce) with them. Shu and Liu (2019) estimated that, in the Dalucao carbonatites, hydrothermal bastnäsite-(Ce) formed between 147°C and 323°C while the pervasive hydrothermal bastnäsite-(Ce) stage of the Maoniuping carbonatite deposit also crystallised at low temperature, between 160°C to 240°C (Zheng and Liu, 2019). Both these studies invoke a fluid with high (SO₄)⁻² content, alongside Cl⁻ and F⁻. It should be noted that the similarity in oxygen isotope composition between different quartz generations (Table 4) suggests that the hydrothermal fluid from which they grew had an oxygen composition dominated by interaction with magmatic silicates under similar conditions to those at which the hydrothermal quartz was precipitated.

Possible sources of hydrothermal fluids and their dissolved components

This investigation has demonstrated that the fluid inclusions in the hydrothermal quartz (Qz-2 and Qz-3) are very variable. Where solids are present they vary in both abundance and mineralogy between adjacent inclusions. The ratio of CO₂ vapour phase to aqueous fluid is also variable. We also note that the sulfate-rich fluid could not have also transported all the associated cations, as baryte and celestine are nearly insoluble (Blount, 1977; Monnin, 1999). We conclude from these lines of evidence that the population of solid-bearing inclusions results from heterogeneous trapping, but the issue of how such a complex, multi-phase fluid came to be present must still be explained.

We note however that similar CO₂-bearing fluid inclusions with sulfate solids and opaque crystals hosted in quartz and calcite from a quartz-bearing carbonatite deposit in the north Qinling region were attributed by Song *et al.* (2016) to trapping of a carbonatite fluid exsolved at subsolidus conditions. Sulfate-rich

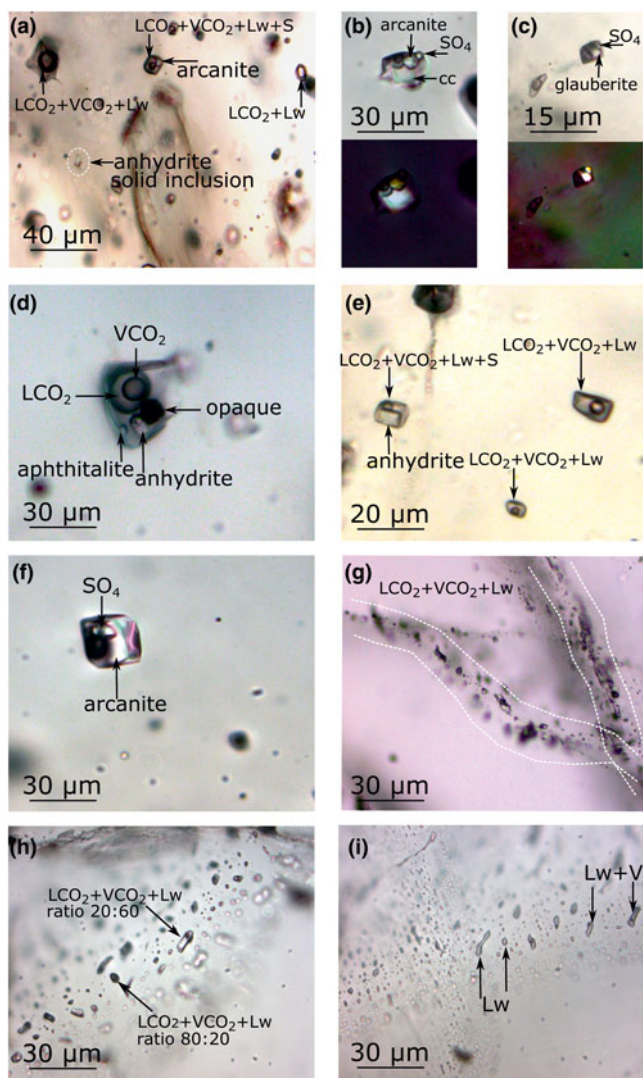


Fig. 6. Microphotographs of fluid inclusions hosted in Qz-2 (a–f) and Qz-3 (g–i). (a) $\text{LCO}_2 + \text{VCO}_2 \pm \text{Lw} \pm \text{S}$ fluid inclusions hosted in cloudy quartz showing variation of the CO_2 and aqueous phase ratio, the fluid inclusion on the top right show the gas bubble taking up most of the fluid inclusions volume while the fluid inclusion in the top middle show a rather small gas bubble, with a homogenised CO_2 -bearing fluid inclusions ($\text{LCO}_2 \pm \text{Lw}$). The $\text{LCO}_2 + \text{VCO}_2 \pm \text{Lw} + \text{S}$ inclusion contains an arcanite solid. Note the anhydrite solid inclusion in the quartz has a similar size to the trapped solid (DSG 002 4). (b) $\text{LCO}_2 + \text{VCO}_2 \pm \text{Lw} + 3\text{S}$ fluid inclusion hosting sulfate and calcite solids (DSG 433 2f) with the corresponding cross polar image. (c) $\text{LCO}_2 + \text{VCO}_2 \pm \text{Lw} + 2\text{S}$ fluid inclusion hosting two sulfate solids and a $\text{LCO}_2 \pm \text{Lw}$ fluid inclusion (DSG 437 8i) with the corresponding cross polar image. (d) $\text{LCO}_2 + \text{VCO}_2 \pm \text{Lw} + 4\text{S}$ fluid inclusions clearly showing the CO_2 vapour bubble within the CO_2 liquid. The fluid inclusion hosts two identified sulfates, one unidentified solid and one opaque (DSG 433 2a). (e) Three $\text{LCO}_2 + \text{VCO}_2 \pm \text{Lw} \pm \text{S}$ fluid inclusions cluster with one with a trapped anhydrite solid (DSG 002 13a). (f) $\text{LCO}_2 + \text{VCO}_2 \pm \text{Lw} + 2\text{S}$ fluid inclusion hosting two sulfate solids, similar to (b) most of the space is taking up by the solids (DSG 433 4d). (g) Thin healed fractures hosting $\text{LCO}_2 + \text{VCO}_2 \pm \text{Lw}$ fluid inclusions cross cutting fluid-inclusion free Qz-1 (DSG 437). (h) $\text{LCO}_2 + \text{VCO}_2 \pm \text{Lw}$ fluid inclusions in a planar array showing variation of the CO_2 and aqueous phase ratio (DSG 433 33b). (i) Wide healed fracture hosting Lw and Lw + V in the same planar array (DSG 433 29). Abbreviations: ‘cc’ – calcite; ‘ SO_4 ’ – unidentified sulfate phase.

fluids have also been found in the Maoniuping REE deposit, from the Himalayan orogenic belts, China within a similar carbonatite setting (Xie *et al.*, 2009, 2015). They described extremely sulfate-rich melt-fluid inclusions in fluorite and suggested a sulfate-rich supercritical orthomagmatic fluid originated from

the unmixing of the carbonatite melt. Alkali-sulfate salt melt inclusions have been identified in carbonatites by Panina and Motorina (2008).

There are two difficulties in applying these models to the examples described here. Firstly the heterogeneous character of the inclusions makes it very unlikely that their contents correspond to any single fluid. Secondly, at Dashigou, no melt inclusions or other sulfate-rich phases are present in the early, high temperature Qz-1. Instead, we infer that the variety of the fluid inclusions provides evidence for at least three different types of fluids associated with hydrothermal Qz-2 and Qz-3: a sulfate-rich aqueous fluid, a more dilute aqueous fluid and a carbonic fluid. Although the sulfate content of these hydrothermal fluids might have been derived directly from a carbonatite parent, this cannot be demonstrated, and it is possible that the sulfate is derived from oxidation of reduced sulfur under surface conditions. Acid sulfate geothermal waters are common in many modern volcanic geothermal systems formed at similar temperatures to those inferred for the hydrothermal activity here (Lewis *et al.*, 1997; Smith *et al.*, 2010). Boiron *et al.* (1999) described sulfate-rich fluid inclusions associated with retrograde quartz veins from Ouro Fino (Brazil) and pointed out that the composition of the fluid was similar to some present day geothermal systems where feldspars have been destroyed and so cannot buffer the Na/K ratio. However, S isotope data from sulfides and sulfates are consistent with a magmatic sulfur source with $\delta^{34}\text{S}$ of $\sim 1\%$ (Huang *et al.*, 1984; Song *et al.*, 2016).

The more dilute fluid present in many Qz-3 fluid inclusions is also consistent with the introduction of a fluid of geothermal origin, as it is common in modern geothermal fields for fluids with different ligand concentrations to occur within the same system (Henley and Hedenquist, 1986; Lewis *et al.*, 1997).

The carbonic fluid observed in the majority of the fluid inclusions hosted in Qz-2 and Qz-3 could have resulted from the dissolution of calcite within the carbonatite (Fig. 10, model 1). Nonetheless, CO_2 -rich fluids have also been commonly described as orthomagmatic fluids resulting from carbonatite magma unmixing (Rankin, 2005; Böhn *et al.*, 2002).

It is unlikely that metal and sulfate ions now present in Qz-2 inclusions were introduced in a single fluid. It is clear from the varied mineralogy of the inclusions that the proportions of major cations in sulfate inclusions are very variable, and in any case the bulk fluid composition cannot have existed as a single phase under the conditions inferred for the hydrothermal activity, if at all. The Maoniuping REE carbonatite deposit host sulfate-rich multisolid daughter-crystal fluid inclusions (Xie *et al.*, 2015; e.g. ADC and ADV fluid inclusions), which behaved differently as they did meet the expectations for a single-phase origin. However, unlike these fluid inclusions, none of the CO_2 -bearing fluid inclusions at Dashigou homogenised upon heating, which is evidence for heterogeneous trapping.

Model for the hydrothermal alteration at Huanglongpu

Two possible models for the hydrothermal alteration and HREE enrichment of the calcite carbonatites at Dashigou, based on inclusion mineralogy and fluid-inclusion results are presented in Fig. 10. They are intended to demonstrate how a sulfate-rich fluid is able to interact with a source of cations to produce a multi-phase fluid.

Model 1 is based on the reaction of a single acid sulfate fluid with the calcite carbonatite and its hosts. This generates CO_2

		Magmatic stage	Qz-2	Qz-3
			early hydrothermal	late hydrothermal
REE minerals (after Smith <i>et al.</i> , 2018)	Monazite	██████████		
	Bastnäsite	██████████		
	Parisite	██████████	██████████	
	Burbankite	██████████		
	Apatite	██████████		
	Britholite		██████████	
	Allanite		██████████	
	Synchysite			██████████
	Röntgenite			██████████
Fluid inclusion types	LCO ₂ +VCO ₂ +Lw		██████████	
	LCO ₂ +VCO ₂ +Lw±S(s)			
	Lw+V/Lw			██████████
Sulfate occurrence	SO ₄ in sol		██████████	
	SO ₄ solid in FI		██████████	
	SO ₄ inclusion in qz		██████████	
Major gangue minerals	Calcite	██████████		
	Celestine-baryte			

Fig. 7. Simplified paragenetic diagram illustrating the paragenetic sequence associated to the later quartz generations in the Huanglongpu carbonatites. The REE minerals paragenesis is after Smith *et al.* (2018). Bar thickness represents minerals and fluid inclusions abundance. Abbreviations: 'FI' – fluid inclusion; 'qz' – quartz.

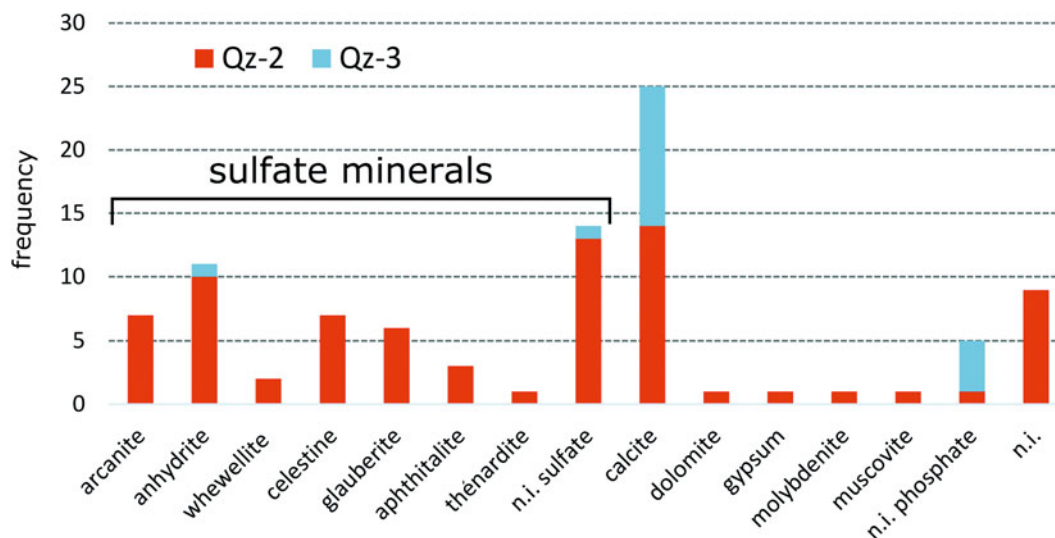


Fig. 8. Frequency histogram showing the different minerals identified by Raman spectroscopy within the fluid inclusions and hosted as solid inclusion in the quartz in Qz-2 and Qz-3. Abbreviation: 'n.i.' is 'non-identified'. Note that the celestine/glauberite spectra are counted in the 'n.i. sulfate' bar.

and precipitate sulfates by the neutralisation of the acid fluid by wallrock reactions (e.g. $\text{H}_2\text{SO}_4 + \text{CaCO}_3 = \text{CaSO}_4 + \text{CO}_2 + \text{H}_2\text{O}$). The sulfate minerals present in the fluid inclusions and in quartz are mainly salts of K (arcanite), Ca (anhydrite), Sr (celestine) and Na (apthitalite) (Fig. 9), and these cations are readily available within wallrock calcite carbonatite dykes or the surrounding fenite (e.g. $\text{H}_2\text{SO}_4 + 2\text{KAlSi}_3\text{O}_8 = \text{K}_2\text{SO}_4 + \text{Al silicates}$). In this model, local production of CO_2 explains why it is associated closely with the sulfate fluid.

Model 2 involves the mixing of two externally-derived fluids, one sulfate-rich and one CO_2 -rich, with cations carried by the carbonic fluid, and does not explicitly require chemical interaction with the carbonatite or fenite. This model can also result in the precipitation of sulfate salts, but requires cations to be introduced in a carbonic fluid even though they, and the CO_2 , are already available in the rocks.

Irrespective of the origin of the initial alteration and precipitation of sulfates, the growth of Qz-3 appears to be associated with the introduction of a more dilute fluid to the system and this is also shown in Fig. 10.

While Qz-2 occurs as thread-like infills linked by a cobweb texture, Qz-3 always occurs infilling healed fractures (Fig. 4). We propose a late fracturing event led to the introduction of the more dilute water, leading to Qz-3 precipitation and the less saline fluid inclusions. Loss of CO_2 at this stage is likely as aqueous Lw + V and Lw fluid inclusions become common (Fig. 10).

Hydrothermal REE enrichment

The HREE enrichment of the Dashigou carbonatite leading to the uncommon flat REE pattern (Fig. 3) is believed to be due to a combination of factors. Smith *et al.* (2018) proposed a

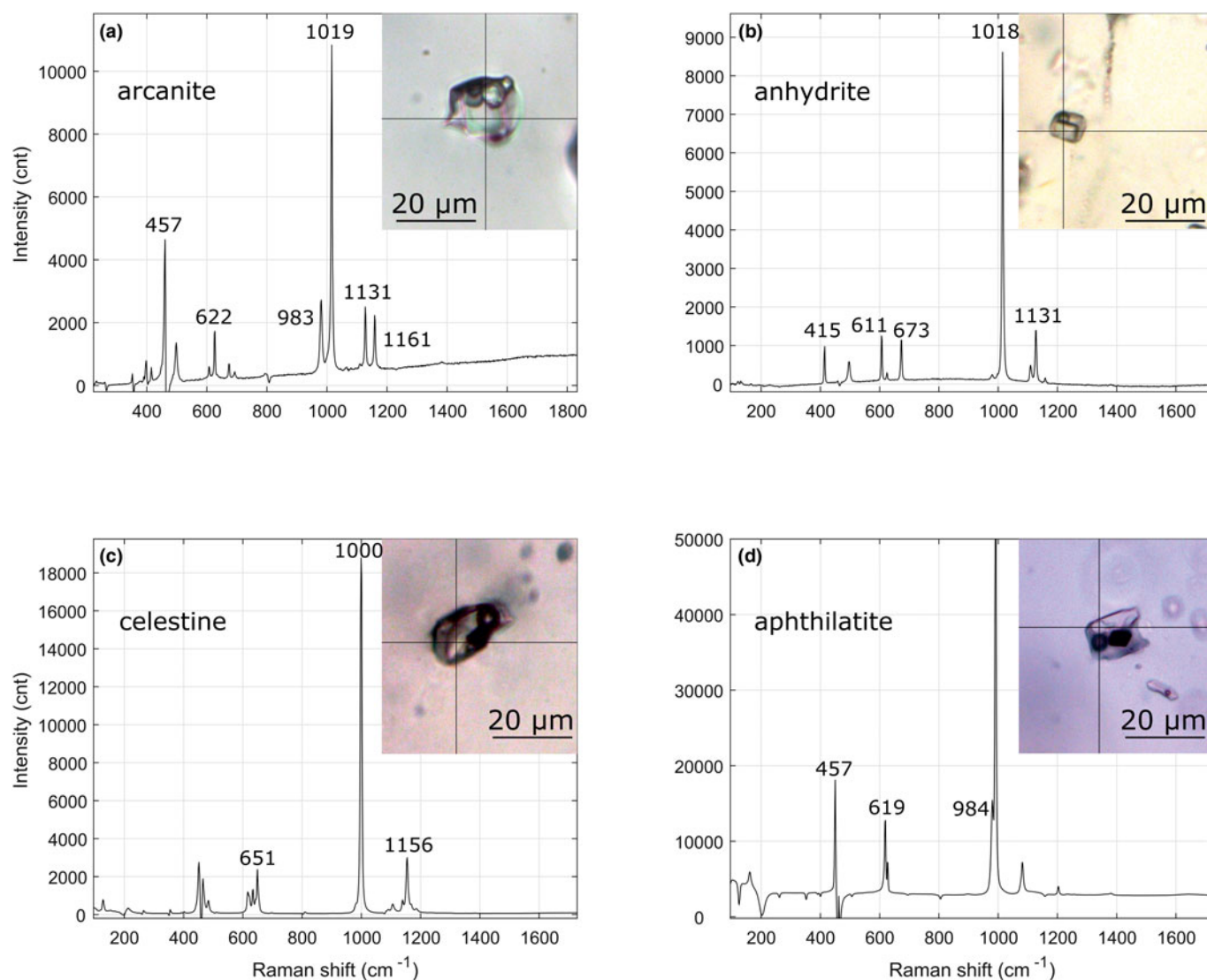


Fig. 9. Laser Raman spectroscopy spectra of some trapped solids hosted in Qz-2 fluid inclusions from the Dashigou calcite carbonatites note that the background signal from the quartz were subtracted. (a) Arcanite spectrum of a $\text{LCO}_2 + \text{VCO}_2 + \text{Lw} + 3\text{S}$, the solid on the right is calcite and the solid in the middle is an unidentified sulfate solid (DSG 433 2f-1). (b) Anhydrite spectrum of a $\text{LCO}_2 + \text{VCO}_2 + \text{Lw} + \text{S}$ (DSG 002 13a-1). (c) Celestine spectrum of a $\text{LCO}_2 + \text{VCO}_2 + \text{Lw} + 2\text{S}$, the celestine crystal is accompanied with an unidentified opaque (DSG 437 8b-1). (d) Aphthilatite spectrum in a $\text{LCO}_2 + \text{VCO}_2 + \text{Lw} + 3\text{S}$, the opaque and the small transparent solid are unidentified (DSG 433 6a).

HREE-enrichment model in which magmatic, *HREE*-enriched calcite with a relatively flat *REE* pattern (their fig. 7a) provided a baseline source for the secondary *REE* mineralisation. The magmatic calcite has lower *REE* contents than the magmatic *REE* phases, but it accounts for over 50% of the carbonatite deposit and is more reactive than the *REE* minerals, making calcite a viable *HREE*-enriched source. The primary magmatic *LREE*-rich mineralisation consisted of monazite-(Ce) (e.g. sample HLP15, $\Sigma\text{LREE}/(\text{HREE} + \text{Y}) = 587470$, table 4) and fluorocarbonate (bastnäsite-(Ce) and parisite-(Ce)) mineralisation. These early *REE* minerals show steep, *LREE* enriched, chondrite-normalised patterns as demonstrated by their high $\Sigma\text{LREE}/(\text{HREE} + \text{Y})$ ratio (Smith *et al.*, 2018; fig. 8A–B). The sulfate-rich fluid leached the *REE* from the magmatic carbonatite without fractionation and then precipitated secondary *HREE*-enriched phases with flat *REE* patterns (e.g. britholite-(Ce), Smith *et al.*, 2018; sample HLP10, $\Sigma\text{LREE}/(\text{HREE} + \text{Y}) = 11$, fig. 8C–E; table 6). The

hydrothermal *REE* minerals are still Ce-dominant but have much higher *HREE* content than found typically in carbonatite related systems.

Hydrothermal Qz-2 and Qz-3 grew alongside secondary *REE* minerals as the carbonatites became enriched in *HREE* (Smith *et al.*, 2018), suggesting that the fluid inclusions contain information about the fluid responsible for the *REE* transport and deposition. The associated fluid inclusions have high sulfate contents and Qz-2 and Qz-3 emplacement correlates overall with widespread growth of sulfate minerals and deposition of secondary quartz in the calcite carbonatite dykes.

Rare earth element transport is also likely to be an important factor for *HREE*-enrichment. Migdisov and Williams-Jones (2008, 2014) and Migdisov *et al.* (2016) identified two categories, ligands leading to *REE* transportation (Cl^- and SO_4^{2-}) and ligands leading to *REE* deposition (F^- , OH^- , CO_3^{2-} , HCO_3^- and PO_4^{2-}). At Dashigou, sulfate is inferred to be the main complexing agent

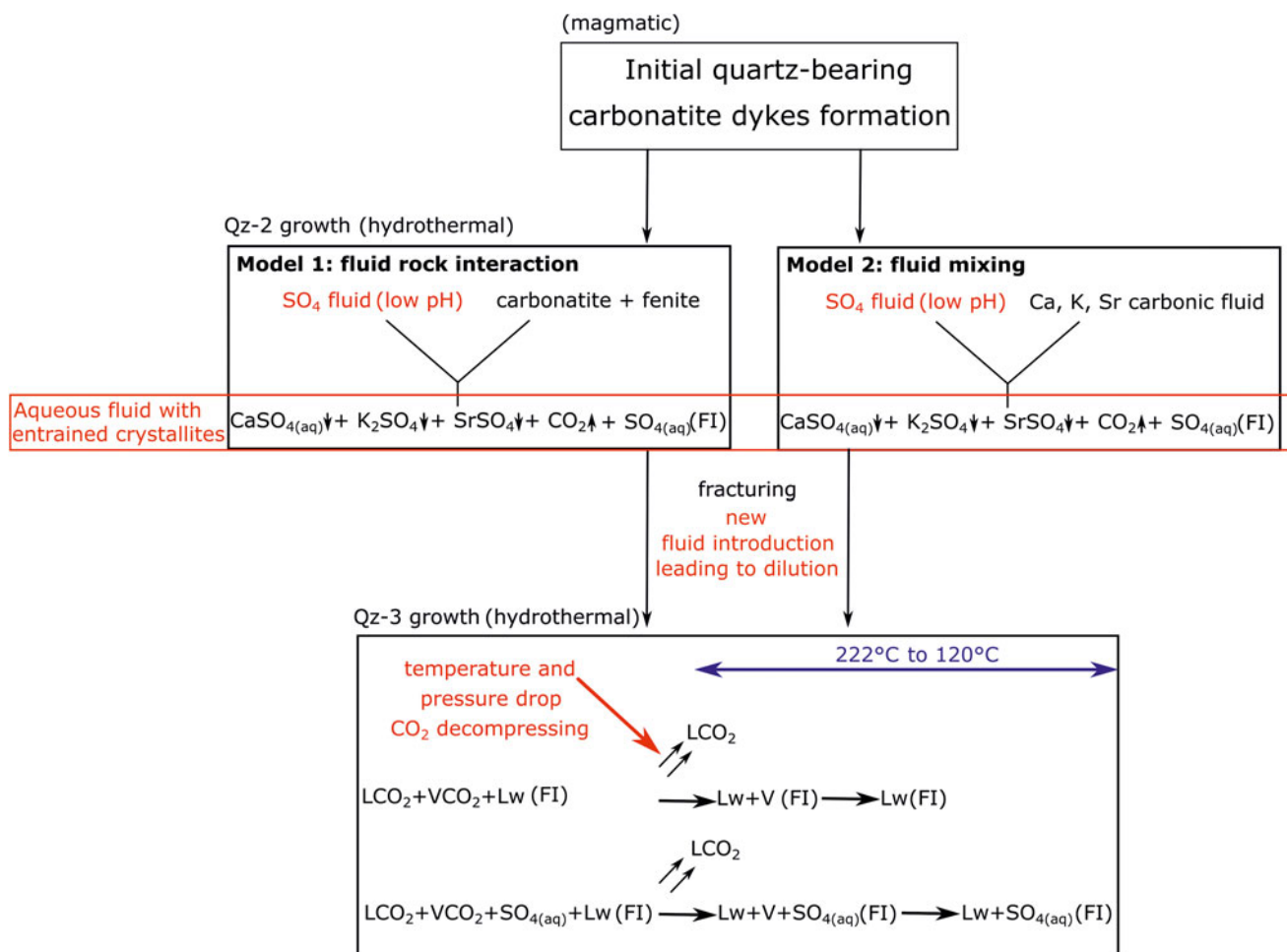


Fig. 10. Potential models for the origin of the fluid inclusions cogenetic with the *HREE* mineralisation in the calcite carbonatite dykes at the Dashigou open pit.

for *REE* transport from the fluid-inclusion data. The flat *REE* profile of the hydrothermally altered calcite carbonatites (Fig. 3) is consistent with experimental studies on the *REE*-SO₄²⁻ complexes at hydrothermal temperatures from 100°C to 400°C (Migdisov and Williams-Jones, 2008, 2014; Migdisov et al., 2016). These studies agree that sulfate is a non-selective ligand as it does not fractionate the *LREE* from the *HREE*. The stability of *REE*-SO₄²⁻ complexes is not strongly dependent on atomic number and they have similar formation constants across the lanthanide series. In contrast, *HREE*-Cl²⁺ complexes show an overall lower stability than *REE*-sulfate complexes and as this decreases along the lanthanide series, a chloride-dominated fluid will fractionate the *LREE* from the *HREE*. In contrast a sulfate fluid is able to transport the *LREE* and the *HREE* equally. One case study on a natural carbonatite system has demonstrated previously the importance of *REE* sulfate transport at low temperature below 240°C (Zheng and Liu, 2019). Sulfate transport has also been observed in sedimentary basin systems at low hydrothermal temperature between 100°C and 120°C (Richter et al., 2019).

The chloride content of the Dashigou fluids were not measured but no trace of Cl-bearing salts were observed suggesting only a minor amount of this ligand is present in the fluids. The precipitation of sulfate minerals within the calcite carbonatite dyke as the sulfate fluid encountered Ca, Na and K is inferred to have destabilised the *REE*-SO₄²⁻ complexes and triggered the

deposition of the hydrothermal *REE* minerals. While sulfate transport does not account for the *HREE* enrichment specifically, it plays an important role in linking *REE* mineralisation to the growth of sulfate minerals.

The final *HREE* enrichment factor is thought to be the stabilisation of secondary minerals whose crystal structures tend to favour *HREE*, in particular *HREE*-enriched fluorocarbonates, uraninite, xenotime-(Y), churchite-(Y) and other minerals which were not always possible to identify; Smith et al. (2018) also reported britholite-(Ce) and Ca-*REE* fluorocarbonate mineralisation. These fractionate the *HREE* out of the fluid they are crystallising from. An additional mechanism that could also have concentrated the *HREE* is the co-precipitation of hydrothermal gangue *LREE* enriched phase such as sulfate minerals.

In summary, a *HREE*-enriched source is probably important for the final *HREE* enrichment. The late-stage magmatic *HREE* enrichment of the calcite, the main gangue mineral of the carbonatite, provides a source baseline allowing a potential secondary *HREE* enrichment (Xu et al., 2007; Smith et al., 2018; Bai et al., 2019). However, it is also possible that *HREE*-enrichment is enhanced at the hydrothermal stage. This might have happened indirectly, by selective removal of *LREE* in a Cl fluid (Smith et al., 2018), although no evidence for such a fluid has been seen, or directly through transport and precipitation of *REE*. Sulfate-*REE* complexation facilitates non-selective transport of the *REE*, and

precipitation of *REE* minerals might then occur in response to precipitation of sulfate minerals. Stabilisation of secondary *HREE*-enriched minerals in the hydrothermal environment could have selectively concentrated *HREE*.

Conclusions

The calcite carbonatites at Dashigou can be divided into two groups on the basis of hydrothermal alteration of magmatic minerals, including monazite-(Ce); little-altered calcite carbonatites exhibit a normal carbonatite *LREE*-enriched *REE* pattern, but more altered dykes have enhanced levels of *HREE* and show an unusual flat *REE* pattern (Fig. 3). These observations suggest that the rocks became enriched in *HREE* in the course of the hydrothermal alteration which was accompanied by the growth of secondary minerals which favoured incorporation of *HREE* (Smith *et al.*, 2018). Alteration took place in at least two phases whose conditions are not well-defined but are between 450°C and 120°C. The hydrothermal fluid responsible for the alteration was remarkably sulfate-rich, and the bulk composition of heterogeneously-trapped fluid inclusions can exceed 30 wt.% K₂SO₄ equivalent. The *REE* were transported as sulfate complexes and probably precipitated due to the precipitation of sulfate gangue minerals. The simplest model for the process involves interaction of an externally-derived acid sulfate hydrothermal fluid with carbonatite and fenite (Fig. 10). Calcite and silicates neutralised the acidity of the sulfate-rich fluid, generating CO₂ and acquiring cations (K, Ca and Na) that precipitated sulfates. Late fracturing was accompanied by renewed quartz precipitation from a more dilute fluid lacking CO₂.

Overall, the *HREE* enrichment of the Dashigou carbonatite is believed to be due to a combination of factors. Late-magmatic *HREE* enrichment of the calcite, the main mineral of the carbonatite, provided a source baseline. Secondary *HREE*-enrichment was made possible by a fluid rich in sulfate, a non-selective *REE* ligand able to transport and concentrate the *REE* equally, but in complexes that are destabilised by the precipitation of sulfate minerals. Final *HREE*-enrichment was achieved by the growth of secondary *REE* minerals which favour *HREE*, notably *HREE*-enriched fluorocarbonates, uraninite, xenotime-(Y) and churchite-(Y).

Supplementary material. To view supplementary material for this article, please visit <https://doi.org/10.1180/mgm.2019.78>.

Acknowledgements. We thank Richard Walshaw and Duncan Hedges for help with the SEM imaging and the EPMA analyses at the University of Leeds. We are grateful to John Craven for the help with the SIMS analyses. Cheng Xu and Song Wei (University of Peking) organised access to the Dashigou open pit and guided us in the field. Finally, thanks to Marie-Camille Caumont from the University of Lorraine, who supervised the Raman spectroscopy analyses. This work was supported by the NERC SoS:RARE project (NE/M01147X/1) and NERC and the British Geological Survey (IMF639/1017).

References

Andersen A.K., Clark J.G., Larson P.B. and Neill O.K. (2016) Mineral chemistry and petrogenesis of a HFSE(+*HREE*) occurrence, peripheral to carbonatites of the Bear Lodge alkaline complex, Wyoming. *American Mineralogist*, **101**, 1604–1623.

Bai T., Chen W. and Jiang S. (2019) Evolution of the carbonatite Mo–*HREE* deposits in the Lesser Qinling Orogen: Insights from *in situ* geochemical investigation of calcite and sulfate. *Ore Geology Reviews*, **113**, 1–14.

Blount C. (1977) Baryte solubilities and thermodynamic quantities up to 300°C and 1400 bars. *American Mineralogist*, **62**, 942–957.

Boiron M.-C., Moissette A., Cathelineau M., Banks D., Monin C. and Dubessy J. (1999) Detailed determination of paleofluid chemistry: an integrated study of sulfate-volatile rich brines and aqueo-carbonic fluids in quartz veins from OuroFino (Brazil). *Chemical Geology*, **154**, 179–192.

Bühn B., Rankin A.H., Schneider J. and Dulski P. (2002) The nature of orthomagmatic, carbonatitic fluids precipitating *REE*, Sr-rich fluorite: fluid-inclusion evidence from the Okorusu fluorite deposit, Namibia. *Chemical Geology*, **186**, 75–98.

Cangelosi D.A., Broom-Fendley S., Banks D.A., Morgan D.J. and Yardley B.W.D. (2019) *LREE* redistribution during hydrothermal alteration at the Okorusu carbonatite complex, Namibia. *Mineralogical Magazine*, <https://doi.org/10.1180/mgm.2019.54>

Chakhmouradian A.R. and Wall F. (2012) Rare earth elements: Minerals, mines, magnets (and more). *Elements*, **8**, 333–340.

Chakhmouradian A.R. and Zaitsev A.N. (2012) Rare earth mineralisation in igneous rocks: Sources and processes. *Elements*, **8**, 347–353.

Dubessy J., Poty B. and Ramboz C. (1989) Advances in C–O–H–N–S fluid geochemistry based on micro-Raman spectrometric analysis of fluid inclusions. *European Journal of Mineralogy*, **1**, 517–534.

European Commission (2017) *The European Economic and Social Committee and the Committee of the Regions on the 2017 List of Critical Raw Materials for the EU*. Communication from the commission to the European parliament, the council. Pp. 490.

Henley R.H. and Hedenquist J.W. (1986) Introduction to the geochemistry of active and fossil geothermal systems. Pp. 1–22 in: *Guide to the active epithermal (geothermal) systems and precious metal deposits of New Zealand* (R.W. Henley, J.W. Hedenquist and P.J. Roberts, editors). Monograph Series Mineral Deposits, Berlin–Stuttgart, Gerbruder Borntrager.

Huang D.H., Wang Y., Nie F. and Jiang X. (1984) Isotopic composition of sulfur, carbon and oxygen and source material of the Huanglongpu carbonatite vein-type of molybdenum (lead) deposits. *Acta Geologica Sinica*, **63**, 252–264 [in Chinese with English abstract].

Huang D.H., Wu C.Y., Du A.D. and He H.L. (1994) Re–Os isotope age of molybdenum deposits in East Qinling and their significance. *Mineral Deposits*, **13**, 221–230 [in Chinese with English abstract].

Kynický J., Smith M.P. and Xu C. (2012) Diversity of rare earth deposits: The key example of China, *Elements*, **8**, 361–367.

Laetsch T and Downs R (2006) *Software For Identification and Refinement of Cell Parameters From Powder Diffraction Data of Minerals Using the RRUFF Project and American Mineralogist Crystal Structure Databases*. Abstracts from the 19th General Meeting of the International Mineralogical Association, Kobe, Japan, 23–28 July 2006.

Lewis A.J., Palmer M.R., Sturchio N.C. and Kemp A.J. (1997) The rare earth element geochemistry of acid-sulfate and acid-sulfate-chloride geothermal systems from Yellowstone National Park, Wyoming, USA. *Geochimica et Cosmochimica Acta*, **61**, 695–706.

Mao J.W., Xie G.Q., Bierlein F., Qu W.J., Du A.D., Pirajno F., Guo B.J., Li Y.F. and Yang Z.Q. (2008) Tectonic implications from Re–Os dating of Mesozoic molybdenum deposits in the East Qinling–Dabie orogenic belt. *Geochimica et Cosmochimica Acta*, **72**, 4607–4626.

McDonough W.F. and Sun S. (1995) The composition of the earth. *Chemical Geology*, **120**, 223–253.

Midende G., Boulvais P., Tack L., Melcher F., Gerdes A., Dewaele S., Demaiffe D. and Decrée S. (2014) Petrography, geochemistry and U–Pb zircon age of the Matongo carbonatite Massif (Burundi): Implication for the Neoproterozoic geodynamic evolution of Central Africa. *Journal of African Earth Sciences*, **100**, 656–674.

Migdisov A.A. and Williams-Jones A.E. (2008) A spectrophotometric study of Nd(III), Sm(III) and Er(III) complexation in sulfate-bearing solutions at elevated temperatures. *Geochimica et Cosmochimica Acta*, **72**, 5291–5303.

Migdisov A.A. and Williams-Jones A.E. (2014) Hydrothermal transport and deposition of the rare earth elements by fluorine-bearing aqueous liquids. *Mineralium Deposita*, **49**, 987–997.

Migdisov A.A., Williams-Jones A.E., Brugger J. and Caporuscio F.A. (2016) Hydrothermal transport, deposition, and fractionation of the *REE*: experimental data and thermodynamic calculations. *Chemical Geology*, **439**, 13–42.

- Monnin C. (1999) A thermodynamic model for the solubility of barite and celestine in electrolyte solutions and seawater to 200°C and to 1 kbar. *Chemical Geology*, **153**, 187–209.
- Panina L.I. and Motorina I.V. (2008) Liquid immiscibility in deep-seated magmas and the generation of carbonatite melts. *Geochemistry International*, **46**, 448–464.
- Rankin A.H. (2005) Carbonatite-associated rare metal deposits – Composition and evolution of ore-forming fluids – The fluid inclusion evidence. Pp. 299–314 in: *Rare-Element Geochemistry and Mineral Deposits* (R.L. Linnen and I.M. Samson, editors). Short Course Notes **17**, Geological Association of Canada, Quebec.
- Ratschbacher L., Hacker B.R., Calvert A., Webb L.E., Grimmer J.C., McWilliams M.O., Ireland T., Dong S. and Hu J. (2003) Tectonics of the Qinling (Central China): Tectonostratigraphy, geochronology, and deformation history. *Tectonophysics*, **366**, 1–53.
- Richter L., Diamond L.W., Atanasova P., Banks D.A. and Gutzmer J. (2019) Hydrothermal formation of heavy rare earth (HREE) – xenotime deposits at 100°C in a sedimentary basin. *Geology*, **46**, 263–266.
- Rusk B. and Reed M. (2002) Scanning electron microscope-cathodoluminescence analysis of quartz reveals complex growth histories in veins from the Butte porphyry copper deposit, Montana. *Geology*, **30**, 727–730.
- Rusk B.G., Reed M.H., Dilles J.H. and Kent A.J.R. (2006) Intensity of quartz cathodoluminescence and trace-element content in quartz from the porphyry copper deposit at Butte, Montana. *American Mineralogist*, **91**, 1300–1312.
- Shepherd T.J., Rankin A.H. and Alderton D.H.M. (1985) *A Practical Guide to Fluid Inclusion Studies*. Blackie, Glasgow and London.
- Shu X. and Liu Y. (2019) Fluid inclusion constraints on the hydrothermal evolution of the Dalucao Carbonatite-related REE deposit, Sichuan Province, China. *Ore Geology Reviews*, **107**, 41–57.
- Smith M.P., Henderson P. and Campbell L.S. (2000) Fractionation of the REE during hydrothermal processes: Constraints from the Bayan Obo Fe–REE–Nb deposit, Inner Mongolia, China. *Geochimica et Cosmochimica*, **64**, 3141–3160.
- Smith D.J., Jenkin G.R.T., Naden J., Boyce A.J., Petterson M.G., Toba T., Darling W.G., Taylor H. and Millar I.L. (2010) Anomalous alkaline sulfate fluids produced in a magmatic hydrothermal system – Savo, Solomon Islands. *Chemical Geology*, **275**, 35–49.
- Smith M.P., Campbell L.S. and Kynický J. (2015) A review of the genesis of the world class Bayan Obo Fe–REE–Nb deposits, Inner Mongolia, China: Multistage processes and outstanding questions. *Ore Geology Reviews*, **64**, 459–476.
- Smith M., Kynický J., Xu C., Song W., Spratt J., Jeffries T., Brtnický M., Kopriva A. and Cangelosi D. (2018) The origin of secondary heavy rare earth element enrichment in carbonatites: Constraints from the evolution of the Huanglongpu district, China. *Lithos*, **308–309**, 65–82.
- Song W., Xu C., Qi L., Zhou L., Wang L., and Kynický J. (2015) Genesis of Si-rich carbonatites in Huanglongpu Mo deposit, Lesser Qinling orogen, China and significance for Mo mineralization. *Ore Geology Reviews*, **64**, 756–765.
- Song W., Xu C., Smith M.P., Kynický J., Huang K., Wei C., Li Z. and Shu Q. (2016) Origin of the unusual HREE–Mo-rich carbonatites in the Qinling Orogen, China. *Scientific Reports*, **6**, 1–10.
- Stein H.J., Markey R.J., Morgan M.J., Du A. and Sun Y. (1997) Highly precise and accurate Re–Os ages for molybdenite from the East Qinling–Dabie molybdenum belt, Shaanxi province, China. *Economic Geology*, **92**, 827–835.
- Thair A.A. and Olli S. (2013) Geochemistry and mineral phases of REE in Jammi carbonatite veins and fenites, southern end of the Sokli complex, NE Finland. *Geochemistry: Exploration, Environment, Analysis*, **13**, 217–224.
- Trofanenko J., Williams-Jones A.E., Simandl G.J. and Migdisov A.A. (2016) The Nature and Origin of the REE Mineralization in the Wicheeda Carbonatite, British Columbia, Canada. *Economic Geology*, **111**, 199–223.
- Valakovich M.P. and Altunin U.V. (1968) *Thermophysical Properties of Carbon Dioxide*. Collets, London.
- Verplanck P.L. (2017) The role of fluids in the formation of rare earth element deposits. *Procedia Earth and Planetary Science*, **17**, 758–761.
- Verplanck P.L., Farmer G.L., Kettler R.M., Lowers H.A., Koenig A.E. and Blessington M.J. (2014) Rare earth element enrichments in the Elk Creek carbonatite. *Acta Geologica Sinica*, **88**, 466–467.
- Wall F. (2014) Rare earth elements. Pp. 312–340 in: *Critical Metals Handbook* (A. Gunn, editor). Wiley, New York, USA.
- Wall F., Niku-Paavola V.N., Storey C.M. and Axel J.T. (2008) Xenotime-(Y) from carbonatite dykes at Lofdal, Namibia: Unusually low LREE:HREE ratio in carbonatite, and the first dating of xenotime overgrowths on zircon. *The Canadian Mineralogist*, **46**, 861–877.
- Williams-Jones A.E., Migdisov A.A. and Samson I.M. (2012) Hydrothermal mobilisation of the rare earth elements – a tale of “ceria” and “yttria”. *Elements*, **8**, 355–360.
- Woolley A.R. and Kempe D.R.C. 1989. Carbonatites: nomenclature, average chemical composition. Pp. 1–14 in: *Carbonatites: Genesis and evolution* (K. Bell, editor). Unwin Hyman, London.
- Xie Y., Hou Z., Yin S., Dominy S., Xu J., Tian S. and Xu W. (2009) Continuous carbonatitic melt–fluid evolution of a REE mineralization system: Evidence from inclusions in the Maoniuping REE Deposit, Western Sichuan, China. *Ore Geology Reviews*, **36**, 90–105.
- Xie Y., Li Y., Hou Z., Cooke D., Danyushevsky L., Dominy S. and Shuping Yin S. (2015) A model for carbonatite hosted REE mineralisation – the Mianning–Dechang REE belt, Western Sichuan Province, China. *Ore Geology Reviews*, **70**, 595–612.
- Xu C., Campbell I.H., Allen C.M., Huang Z., Qi L., Zhang H. and Zhang G. (2007) Flat rare earth element patterns as an indicator of cumulate processes in the Lesser Qinling carbonatites, China. *Lithos*, **95**, 267–278.
- Xu C., Kynický K., Chakhmouradian A.R., Qi L. and Song W. (2010) A unique Mo deposit associated with carbonatites in the Qinling orogenic belt, central China. *Lithos*, **118**, 50–60.
- Zheng Y.F. (1999) Oxygen isotope fractionation in carbonate and sulfate minerals. *Geochemical Journal*, **33**, 109–126.
- Zheng X. and Liu Y. (2019) Mechanisms of element precipitation in carbonatite-related rare-earth element deposits: Evidence from fluid inclusions in the Maoniuping deposit, Sichuan Province, southwestern China. *Ore Geology Reviews*, **107**, 218–238.